The Photodisintegration of the deuteron close to threshold

F D SMIT

Thesis submitted for the degree of

Doctor of Philosophy at the University of Cape Town

May 1986

The University of Cape Town has been given the right to reproduce this thesis in whole or in part. Copyright is held by the author.

The copyright of this thesis vests in the author. No quotation from it or information derived from it is to be published without full acknowledgement of the source. The thesis is to be used for private study or non-commercial research purposes only.

Published by the University of Cape Town (UCT) in terms of the non-exclusive license granted to UCT by the author.

University of Cape Town

ABSTRACT

Theoretical calculations predict that deuteron photodisintegration is sensitive to meson exchange current and isobar configuration contributions in the threshold (2.225 MeV) region. These effects are manifested chiefly through M1 transitions, which reach maximum amplitude in this energy region. The calculated size of these effects can be verified from an angular distribution measurement of the photoproducts.

The feasibility of making an angular distribution measurement in the threshold energy region was investigated for gamma rays from the $^{14}N(p,p'\gamma)$ reaction as well as from ^{228}Th, ^{72}Ga and ^{24}Na radioactive sources.

A photoneutron angular distribution measurement was made using the 2.75 MeV gamma rays from ^{24}Na. Measurements were made at six angles ranging from 30° to 135°. A value for the dipole cross section ratio, $\sigma_m/\sigma_e = 0.290 \pm 0.021$, was calculated from the measurements. This value is consistent with theoretical calculations which predict that meson exchange currents and isobar configurations lead to a 3.5% enhancement in the total cross section for deuteron photodisintegration at $E_\gamma = 2.75$ MeV.

Acknowledgements

The author wishes to express sincere appreciation to the following :

*Prof F D Brooks, his supervisor, for his help and guidance;

*The staff of the Van De Graaff Group at the NAC for their ever-ready assistance;

*Dr H G Miller for the theoretical calculations and informative discussions;

*Dr W R McMurray, Prof S M Perez and Prof D Aschman for their suggestions and comments;

*Messrs M S Allie and B R S Simpson, his fellow students for their general assistance and friendship;

*Dr D Mingay and his staff of the Van De Graaff Group at the AEC for their help with the initial experiments;

*Mr P A Back who constructed the necessary apparatus;

*Messrs P Groenewald and J Hanekom who prepared the diagrams;

*Miss Z Smit and Miss G Blewett for their help in typing various parts of this manuscript;

*His parents for their support and encouragement of his studies;

*The Gerald Wright Memorial Trust and the South African Council for Scientific and Industrial Research for financial assistance.

TABLE OF CONTENTS

Table 1.1 The static properties of the deuteron (Er84)

Binding energy $B = 2.224579(9)$ MeV	(4 ppm)
Inverse wave number $\alpha^{-1} = R = 4.31896(2)$ fm	(5 ppm)
Magnetic moment $\mu_d = 0.857406(1)$ n.m	(1 ppm)
Radius $r_d = 1.963(4)$ fm	(2 ppt)
Effective range $\rho_{av}(-\varepsilon,\varepsilon) = 1.737(12)$ fm	(7 ppt)
Asymptotic S wave amplitude A_s (average) $= 0.8802(20)$	(2 ppt)
Asymptotic D/S ratio $\eta = 0.0271(4)$	(13 ppt)
Quadrupole moment $Q = 0.28590(30)$	(1 ppt)

These high precision measurements of the strongly interlinked static properties of the deuteron impose constraints on any hypothesis for the NN force. It is for example imperative that any description of the deuteron gives the right binding energy. The binding energy determines the size of the deuteron and therefore also by virtue of the uncertainty principle, the type and amount of exchange allowed.

The ground state of the deuteron is known to be a mixture of S and D states as shown, for example, by the small but non-zero quadrupole moment of the deuteron. The difference between the magnetic moment of the deuteron and the sum of the magnetic moments of the separate neutron and proton is particularly sensitive to the percentage D state admixture (typically estimated at 4-5%, (Ho80)). Since the D state component of the wave function is small, it is the cross terms of the S-D wave function that are expected to be the major contributors to the quadrupole moment.

It is also known (Er84) that the deuteron binding is sensitive to the amount of S-D coupling by virtue of the central force being weak and the D state not contributing to the binding. This shows how strongly interlinked the static properties are and the need for descriptions of the deuteron to comply with the boundaries imposed by these properties. Ericson (Er84) in his paper on the static properties of the deuteron pointed out that even as the nature of the NN force is being re-examined in the light of quantum chromodynamics this still remains true.

The nature of the coupling between electromagnetic radiation and a nuclear system is well understood since its interaction is weak and gauge invariant (Ca85). Photodisintegration of the deuteron (discovered by Chadwick and Goldhaber in 1934 (Ch34)) also has an advantage in that it does not introduce a third distortable particle to the system. These factors make deuteron photodisintegration and its inverse, the n-p radiative capture, convenient reactions for studying the NN force.

The better known and more popular experimental observables, which are measured as a function of photon energy in photodisintegration are the absolute total cross section σ_T, the absolute differential cross sections $\sigma_n(\theta)$ and $\sigma_p(\theta)$ for photoneutrons and photoprotons and the polarisation angular distributions $P_n(\theta)$ and $P_p(\theta)$ of these photoproducts. Relative rather than absolute photoproduct angular distribution measurements are also attractive because they are simpler to make than absolute measurements. In certain circumstances, for example near the threshold,

such relative measurements are also useful and can provide information about meson exchange currents (MEC) and other features of the nuclear force.

Riska and Brown (Ri72) were able to explain the longstanding discrepancy between theory and experiment in the total cross section for n-p radiative capture at thermal energies by explicitly incorporating MEC into their calculations. One would therefore expect that this effect should also manifest itself in deuteron photodisintegration close to threshold (2.2245 MeV). This is born out by calculations of σ_T done by Arenhovel et al. (Ar74) which show an enhancement in the threshold region when MEC and isobar configurations (IC) are explicitly included.

This enhancement can be obtained from a relative photoproduct angular distribution measurement in this energy region as is explained in the next section (section 1.2). It is a measurement such as this to verify the enhancement at an incident photon energy of 2.75 MeV with which this thesis is concerned. A review of previous measurements made at this energy can be found in section 1.3.

1.2 The dipole cross section ratio for deuteron photodisintegration.

The differential cross section for deuteron photodisintegration is given by (Ru60)

$$\sigma(\theta) = a + b\sin^2\theta \pm c\cos^2\theta \pm d\cos\theta\sin^2\theta + e\sin^2\theta\cos^2\theta \quad 1.1$$

where the coefficients a, b, c, d, and e are energy dependent and can be determined from a relative angular distribution measurement. The signs are all (+) for photoprotons and (-) where indicated for photoneutrons. In

equ. 1.1 the last three terms are brought in through the inclusion of higher order multipoles ($L \geq 2$) which give the differential cross section an asymmetry about 90^{o}. Close to threshold however, the M1 and E1 transitions are by far the strongest transitions thus equ. 1.1 may be simplified to

$$d\sigma/d\Omega = a + b\sin^2\theta \qquad 1.2$$

The ratio of the photomagnetic (σ_m) to photoelectric (σ_e) contributions to the total cross section, σ_m/σ_e, is known as the dipole cross section ratio. This ratio can be calculated from a relative angular distribution measurement and equ. 1.2 using

$$\sigma_m/\sigma_e = 3a/2b \qquad (1.3)$$

Considering only the $^3S_1$ ground state of the deuteron, the photomagnetic disintegration gives the photoproducts an isotropic distribution in the centre-of-mass frame because the intermediate $^1S_0$ state has no angular momentum (L=0). For the intermediate $^3P_{0,1}$ state on the other hand the photoelectric disintegration gives a $\sin^2\theta$ form to the angular distribution of the photoproducts with respect to the direction of the incoming gamma rays.

The approximation of considering only M1 and E1 transitions does not reduce the sensitivity of the dipole cross section ratio to MEC and IC effects. Close to threshold, higher order multipole transitions are far weaker than M1 and E1 transitions and MEC and IC effects contribute but a fraction to these higher order transitions. Therefore such effects through higher order multipole transitions at energies close to threshold can be neglected.

Considering only M1 and E1 transitions, by virtue of Siegert's theorem, MEC and IC contributions will be manifested through the M1 transitions. It is in M1 transitions of D state photodisintegration that MEC and IC effects are strongest (Ri72)(Ar74). The dipole cross section ratio is directly "related" (through equ. 1.3) to the effects of MEC and IC.

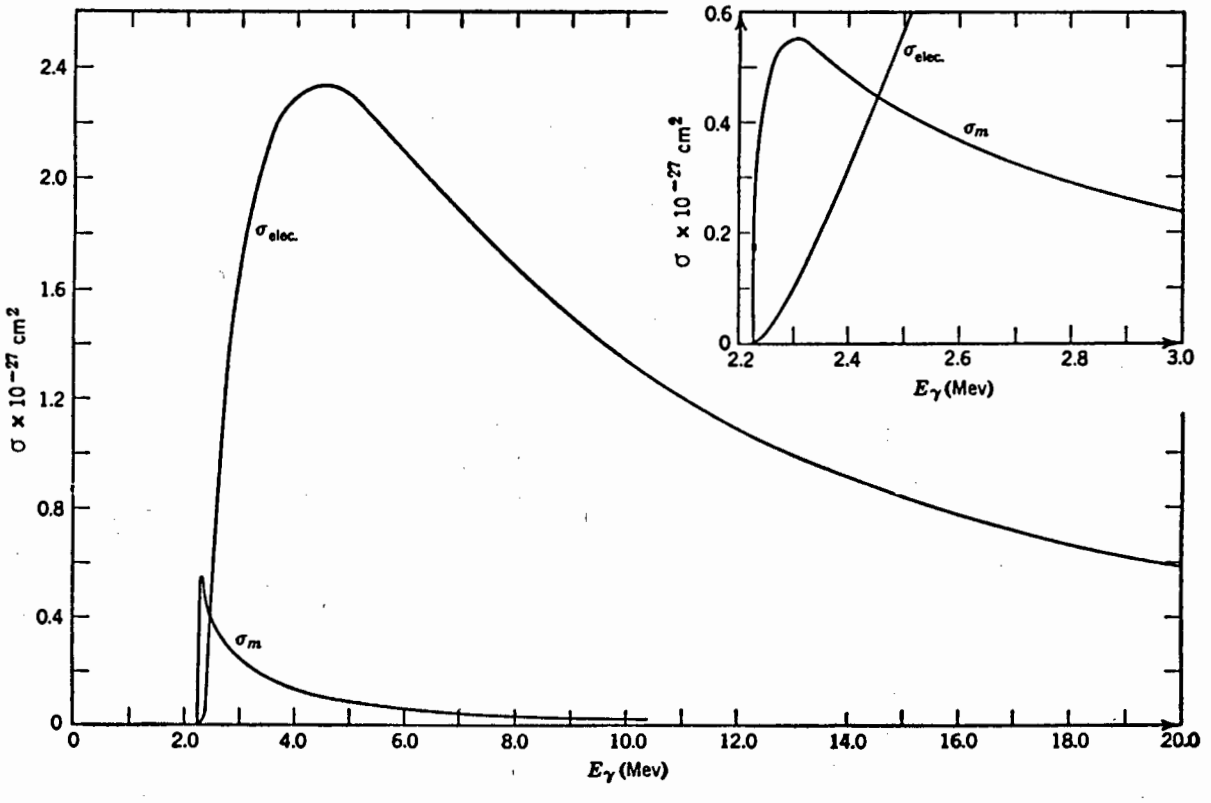

Figure 1.2 The deuteron photomagnetic and photoelectric cross sections calculated from equ. 2.10 and 2.9 respectively. A magnified threshold region is shown in the inset. (Figure from (Be56))

The M1 transition is known to be strong relative to the E1 transition in the threshold region only. At about E_γ = 2.45 MeV (see Fig.1.2) the photoelectric E1 disintegration becomes the bigger contributor to the total differential cross section. These curves represent calculations using the zero range central force approximation for the NN force and

are successful as a first approximation (no D state photodisintegration or MEC and IC) in describing the general trend of data at these energies. This assumes that the deuteron is a point nucleus with only a S ground state and that the NN force has no range.

These aspects are discussed in more detail in chapter 2 where the basis of this description is broadend to include D state contributions.

1.3 Angular distribution measurements made in the threshold region.

Some of the first experiments looking at the angular distribution of photoprotons from deuteron photodisintegration were carried out by Chadwick et al. (Ch37). These experiments were made using a radiothorium source (2.62 MeV gamma rays) and they confirmed the $\sin^2\theta$ component in the angular distribution but were unable to detect the isotropic component from photomagnetic disintegration. In 1942 Myers and Van Atta (My42), using a continuous bremsstrahlung spectrum extending up to 2.43 MeV, demonstrated the existence of the photomagnetic component beyond any doubt.

The angular distribution measurements which followed these early experiments and which aimed to determine the dipole cross section ratio in the threshold region are listed in Table 1.2. From the table can be seen that there was a spate of measurements published beginning in 1949 and abruptly ending in 1951 with the measurements of Bishop et al. (Bi51a). To the best of our knowledge no further angular

distribution measurements in this energy region have been published since that time, a gap of more than thirty years.

This is perhaps surprising in view of the heightened interest in MEC and IC following the work of Riska and Brown (Ri72) and also in view of interest stimulated by the zero degree measurements of the D(γ,n) total cross section at higher energies at Mainz (Hu76). Some photoneutron angular distribution measurements for E_γ = 2.27 - 2.40 MeV made using bremsstrahlung and proton recoil detectors, were reported in the progress reports of the Argonne National Laboratory, 1975 - 1979 (Ja75) (Ja76) (Ja79), but these have not been published.

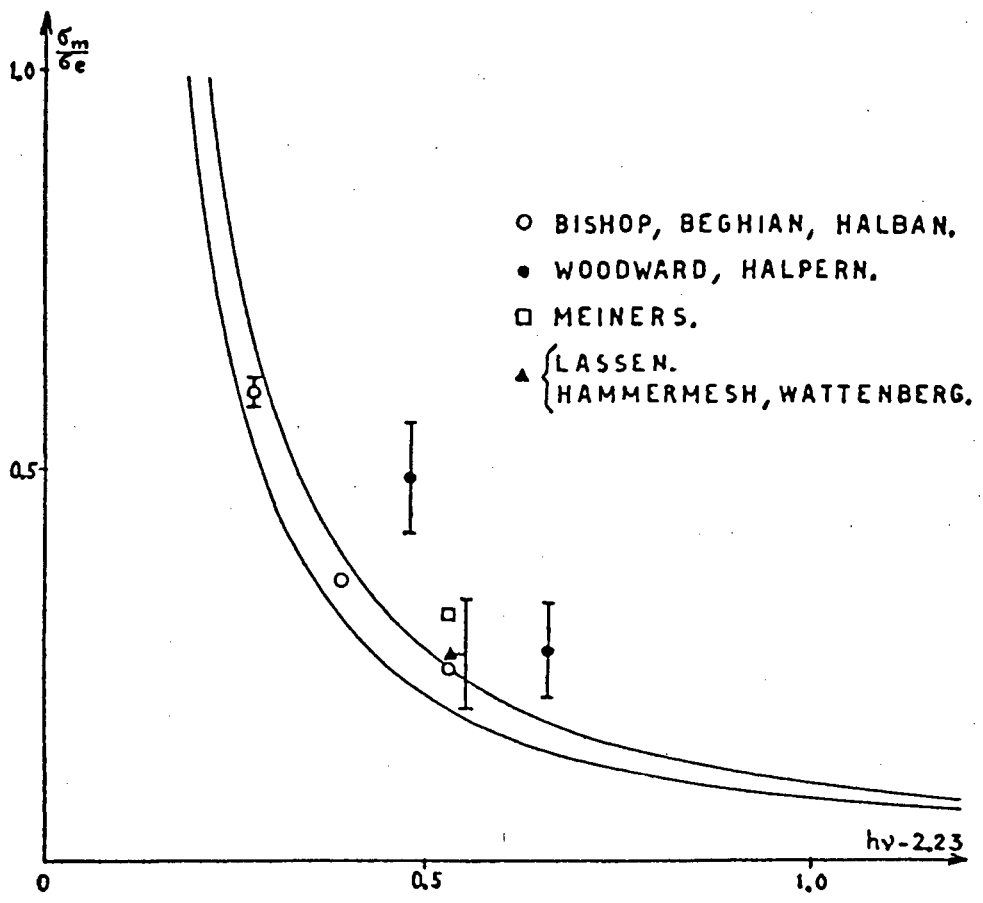

Figure 1.3 A plot of published data in the threshold region together with the limits from calculated σ_m/σ_e ratios. (Figure from (Be50))

The published measurements of σ_m/σ_e are presented in Fig. 1.3 together with the results of calculations by Bethe and Longmire (Be50) which include a tensor component for the nuclear force (to account for the D state) and used effective range theory (chapter 2) to allow for the finite range of the NN force. As can be seen the fit between data and calculation is reasonable. This may have induced some complacency and thereby contributed to the lack of further measurements. According to a recent CINDA reference list (Ci84) for this reaction, the only measurements, other than the total cross section measurements, that have been reported at threshold energies, since 1952, are the photoneutron polarization measurements of Jewell et al. (Je65) at 2.75 MeV.

In reviewing the data on σ_m/σ_e, the experimental methods employed in individual threshold region measurements will be examined (see Table 1.2) noting the techniques used, e.g. the type of target used, whether protons or neutrons were detected, the type of detector used and how scattering corrections, if any, were made.

a. The measurement of Woodward and Halpern (Wo49) employed the end-point method using bremsstrahlung photons. A range telescope of three deuterium filled proportional counters fulfilled the dual role of deuteron target and proton detector. The high gamma flux caused difficulties and led to dc currents of up to 1 μA in the counters. Only forward angles were measured. The experiments with radioactive sources were simpler than this bremsstrahlung

Table 1.2 Summary of D (γ,n) angular distribution measurements in the threshold region

Source and γ-ray Energy MeV	Reference	a/b	σ_m/σ_e	Angles measured (Deg)	p or n detected and method
^{72}Ga	(Bi51)	0.41 ±0.03*	0.61 ±0.04	45 90	n; capture in ^{128}I
2.50	(Bi51a)	0.40 ±0.01*	0.600±0.02	-	p; prop. counters
Th	(Gr45)	0.26 ±0.08	0.39 ±0.13	0 45 90 135 180	n; BF_3 counters
2.62	(Bi51a)	0.240±0.005*	0.360±0.008	-	p; prop. counters
^{24}Na	(Ge49)	0.193±0.024	0.295±0.036	45 60 75 90	n; BF_3 counters
2.75	(Ha49)	0.205±0.05	0.265±0.05	0 90	n; BF_3 counters
	(La49)	0.177±0.043*	0.265±0.065	6 forward angles	p; prop. counters
	(Me49)	0.211±0.008*	0.312±0.012	0 90	n; BF_3 counters
	(Bi51a)	0.165±0.005*	0.247±0.007	-	p; prop. counters
Bremsstrahlung					
2.46	(Wo49)	0.45 ±0.18*	0.67 ±0.27	0 81	p; prop. counters
2.51		0.47 ±0.18*	0.71 ±0.27	0 81	
2.59		0.51 ±0.15*	0.77 ±0.22	0 81	
2.72		0.33 ±0.05	0.49 ±0.07	0 30 45 60 81	
2.90		0.18 ±0.04*	0.27 ±0.06	0 81	

* calculated using equation 1.3

experiment insofar as they used gamma sources which were monoenergetic above the (γ,n) threshold.

b. N.O. Lassen's measurements were first published in 1948 (La48) and corrections to these values were published in 1949 (La49). He made use of a bank of 6 or 7 deuterium filled proportional counters designed so as to detect only the photoprotons emitted parallel to the the counter axis. In this experiment it was therefore impossible to distinguish between protons moving in exactly opposite directions. Symmetry about 90° was assumed when analysing the angular distribution to obtain σ_m/σ_e. Backgrounds caused by the high gamma flux were also a problem in these measurements.

c&d. Both Meiners (Me49) and Genevese (Ge49), detecting photoneutrons, went to great lengths to avoid inscattering in order to reduce the background levels in their experiments. The neutron detectors used in Genevese's experiments and in one of the two independent and different experiments carried out by Meiners consisted of large wax moderators containing embedded BF_3 counters to detect the thermalized neutrons. The large solid angles of these detectors also enhanced their sensitivity to backgrounds from room scattered neutrons.

In Meiners's experiment, the apparatus was mounted on a 16 foot tower extending above the roof of the physics building. Genevese suspended his apparatus from a tethered, hydrogen-filled balloon. Meiners's second experiment used iodine activation techniques based on the Szilard-Chalmers reaction for neutron detection. Meiners's measurements (both

experiments) were limited to only two angles (0° and 90°). They therefore provide no check on the validity of the $\sin^2\theta$ distribution form (equ. 1.2).

Genevese on the other hand made measurements at 4 forward angles. A toroidal sample of heavy water was used by Genevese in his experiments. The toroid was made of a 8 mm diameter copper tube of 0,8 mm thickness. The diameter of the toroid was 10 cm.

The neutron detecting experiments (Ge49)(Me49)(Ha49) all used exptrapolation methods (which would now be considered arbitrary) to correct for the effects of neutron scattering in the heavy water samples. Genevese compared measurements made using D_2O/H_2O mixtures containing different proportions of D_2O. Meiners compared measurements made using spherical D_2O targets with diameters of 0.95, 1.27 and 1.50 cm respectively.

e. Hamermesh and Wattenberg (Ha49) also compared measurements made using D_2O samples of different sizes. Their experiments also used BF_3-in-wax detectors and were confined to measurements at 0° and 90°.

f. The measurements of Bishop et al. (Bi51a) were made using high resolution deuterium filled proportional counters operated at a pressure sufficient to ensure a small wall effect for photoprotons emitted in the $D(\gamma,n)$ reaction. The photoproton angular distribution was then deduced from the measured energy spectrum of the photoprotons by invoking the kinematic relation between energy and angle. These measurements were able, through their ~100% detection efficiency, to obtain much higher statistical accuracy than

other measurements and their final standard deviations are likewise the smallest of all the data published. Unfortunately however, the very brief account published of these measurements (see Appendix A) provides very little scope for speculation about limitations or errors (e.g. systematics which have affected their result.) One notes that their measurement at 2.75 MeV is much lower than other data at this energy. In particular the discrepancy between theirs and the next most accurate measurement at this energy (by Meiners) appears to be irreconcilable.

This discrepancy in the published data together with the thirty year lack of new measurements, the renewed interest in MEC and IC, and the possibility that $L \geq 2$ transitions might be more important than hitherto believed, provided the motivation for making new experimental measurements using modern equipment and techniques at these energies. The interest in MEC and IC together with the disagreement of Bishop's data with current calculations of the size of these and other contributions are discussed in the next chapter.

The experiment eventually devised in response to this motivation was briefly as follows. A ^{24}Na source giving monoenergetic 2.75 MeV gamma rays was used with a deuterated anthracene crystal fulfilling the dual role of a target and photoproton detector. This detector was operated in coincidence with a stilbene crystal which formed the neutron detector in a time-of-flight geometry to reduce background by gating on the photoneutron energy. Both photoproducts were therefore detected giving a clearer photodisintegration

signature than in the earlier experiments which detected either proton or neutron, but not both. Measurements were made at several angles including two backward angles. The technological improvements included nanosecond time-of-flight techniques, pulse shape discrimination (Br59) against gamma background, multiparameter data aquisition and analysis, efficient detection of fast neutrons by proton recoils in scintillators and the use of Monte Carlo calculations to estimate neutron scattering corrections.

CHAPTER 2

Deuteron Photodisintegration theories.

2.1 Introduction.

Quantum mechanical descriptions of the deuteron began with a paper by Bethe and Peierls (Be35) at more or less the same time as experimental measurements were performed. This analysis of the photodisintegration of the deuteron considers the nucleus to be a point particle with no D state contribution or range for the nuclear force and is known as the zero range central force approximation. Changes were made to this description of the NN force by Breit and Condon (Br36) to include its radial dependence and by Rarita and Schwinger (Ra41) include non-central forces.

This description formed the basis to which the effective range of the NN force was added as a correction and to which a further corrections due to meson exchange currents were later also built in (Be50). A more analytical approach was followed until the advent of computers. Henceforth potentials with a more fundamental basis, although still phenomenological, entered into calculations (De59).

The Rustgi paper published in 1960 (Ru60) was aimed at the energy range 20 - 180 MeV. Although the lesser known Signell Marshak potential was used and only transitions up to E2 were included, these calculations form the basis of most of this groups subsequent work in the photodis-integration field. The most comprehensive (computer based) analysis of deuteron photodisintegration was however done by Partovi (Pa64).

It is for these reasons that this chapter has been divided into two parts; namely point nucleon and semi phenomenological calculations. These calculations still did not explicitly include meson exchange currents or isobar configurations. This followed only after the paper by Hadjimicheal (Ha73). There are still however no published calculations of differential cross sections which include meson exchange currents in the threshold region.

2.2 Point nucleon theory.

To arrive at formulae for the differential cross sections for photomagnetic σ_m and photoelectric σ_e disintegration using the zero range central force approximation, there are mainly two methods employed. The direct method of reaching the formulae was used by Bethe and Morrison (Be56) as well as Brown and Jackson (Br74). Both Squires (Sq52), and Blatt and Weisskopf (Bl63) worked out the cross section for neutron proton radiative capture first and then, through time reversal invariance, the differential photodisintegration cross section can be related to the capture cross section by a factor proportional to the square of the ratio of ingoing to outgoing "particle" momenta, (Hw84)

$$d\sigma/d\Omega(n + p \rightarrow d + \gamma) = 1.5(k/p)^2 d\sigma/d\Omega(\gamma + d \rightarrow n + p) \quad 2.1$$

This provides a valuable cross check for theory and experiment for both reactions.

The texts mentioned above give clear accounts of how to reach the cross sections for magnetic or electric dipole absorption in the zero range central force approximation so that here, only the cross sections will be given. Let us

first consider photoelectric disintegration. For photoelectric dipole absorption the total cross section is

$$\sigma_E = \frac{8\pi}{3} \frac{e^2 \hbar B^{\frac{1}{2}} E^{\frac{3}{2}}}{c\, m(E+B)^3} \qquad 2.2$$

where B is the binding energy of the deuteron and E is the final energy of the system i.e. $E = (\hbar\omega - B) \equiv \hbar^2 p^2/m$ and m the reduced mass of an neutron-proton system.

The cross section for photomagnetic disintegration in the zero range central force approximation is

$$\sigma_m = \frac{2\pi}{3} \frac{e^2}{\hbar c} \left(\frac{\hbar}{mc}\right)^2 (\mu_p - \mu_n)^2 \frac{k\gamma\,(1-\gamma a_s)^2}{(k^2+\gamma^2)(1+k^2 a_s^2)} \qquad 2.3$$

where $\gamma = \sqrt{mB/\hbar^2}$ and a_s the scattering length for the S state and μ_p and μ_n the magnetic moments of the proton and neutron respectively. In the equivalent notation of equ. 2.2

$$\sigma_m = \frac{2\pi}{3} \frac{e^2}{\hbar c} \left(\frac{\hbar}{mc}\right)^2 (\mu_p - \mu_n)^2 \frac{BE^{\frac{1}{2}}(B^{\frac{1}{2}} + W_o^{\frac{1}{2}})^2}{(E+B)(E+W_o)} \qquad 2.4$$

where W_o is the energy of the virtual singlet state of the deuteron.

One of the main assumptions made when deriving equ. 2.2 and 2.4 is that the NN force has zero range. Improvements can be made on the zero range central force approximation by using effective range theory first derived by Schwinger (Sc47) for n-p scattering theory. These improvements to the cross sections were made by Bethe and Longmire (Be50) and Feshbach and Schwinger (Fe51).This introduces another parameter with the units of length, namely $\rho(E_1,E_2)$ the effective range, into the system. Effective ranges which differ for singlet and triplet states, are known from n-p scattering data. The effective range paramenter is defined as

$$\rho(E_1,E_2) = 2 \int_o^\infty (U_1 U_2 - \Psi_1 \Psi_2)\, dr \qquad 2.5$$

where Ψ_1 and Ψ_2 are the solutions to the radial Schrödinger

equation for energies E_1 and E_2. Similarly U_1 and U_2 are the asymptotic or the solutions outside the range of the nuclear interaction.

At zero energy the effective range r_o is then

$$\rho(0,E) \simeq \rho(0,0) = r_o = 2 \int_o^\infty (U_o^2 - \Psi_o^2)dr \qquad 2.6$$

at low energies. It can be shown that the "mixed" effective range $\rho(0,E)$ is given by

$$k \cot \delta_s = -\frac{1}{a_s} + \frac{1}{2} k^2 \rho(0,E) \qquad 2.7$$

where δ_s is the S wave phase shift. Equation 2.7 is an approximation of the general equation

$$k \cot \delta_s = -\frac{1}{a} + \frac{1}{2} k^2 r_o - Pk^4 r_o^3 + Q r_o^5 k^6 \qquad 2.8$$

used in effective range theory with P and Q constants. The terms $-Pk^4r^3$ and higher are shape dependent terms which are negligibly small at low energies so that equ. 2.7 is what is used just above the photodisintegration threshold.

A fairly detailed derivation of these equations can be found in a review article on the two nucleon problems by Hulthen and Sugwara (Hu57) as well as others (Sq52) (Mc56). The scattering length a_s and the effective range r_o are determined by the experimental values δ_s and k, the phase shift for the singlet state and k the wave number of the relative motion between the neutron and proton during scattering respectively. This theory is shape independent and so does not specify a particular potential but for an arbitrarily chosen specific potential type and particular values for a and r_o does fix the depth and the range of the potential. According to Bethe and Longmire (Be50), who first used effective range theory for photodisintegration calculations, the photoelectric disintegration cross section

equ. 2.2 is only affected by a factor $(1- r_{ot})^{-1}$ so that (Br74)

$$\sigma_e = \frac{8\pi}{e} \frac{e^2\hbar}{c\ m} \frac{B^{\frac{1}{2}}\ E^{\frac{3}{2}}}{(E+B)^3} \left(\frac{1}{1-r_{ot}}\right) \qquad 2.9$$

The photomagnetic disintegration cross section becomes

$$\sigma_m = \frac{2\pi}{e} \frac{e^2}{\hbar c} \left(\frac{\hbar}{mc}\right)^2 (\mu_p-\mu_n)^2 \frac{[\gamma-a_s^{-1}(k)]^2\ k\gamma}{[k^2+a_s^{-1}(k)]^2(k^2+\gamma^2)(1- r_{ot})} \qquad 2.10$$

The effective range is now denoted by r_{ot} because it is the range of the forces in a triplet state as opposed to that in a singlet state r_{os}.

It was also pointed out in this paper (Be50) that the correction to the photomagnetic disintegration is not as simple and depends on the difference between the triplet and singlet ranges. The factor with which equ. 2.4 must be multiplied is given by (Sa51)

$$R(E) = R(0)x[1+k^2(\tfrac{1}{2}\ r_{os} - D)/(\gamma+\beta'-\gamma^2D)]$$
$$[1+(\tfrac{1}{4}\ r_{os}^2k^4 + \beta' r_{os}k^2)/(k^2 + \beta'^2)], \qquad 2.11$$
$$R(0)=[1-\gamma D/(\gamma+\beta')]^2(1-r_{ot}\gamma)^{-1}(1-\varepsilon_5)^{-1}$$
$$\text{and } D = \tfrac{1}{4}(r_{ot} + r_{os}),\ \beta' = \frac{1}{a_s}$$

in accordance with (Be50) where only $(1-\varepsilon_5)^{-1}$ has been added by (Sa51) to correct for exchange current effects. The variable is the fraction due to the exchange currents of the total cross section for the capture of the neutron by protons. Equation 2.11 is accurate to within 0.5 percent for gamma rays close to threshold (Sa51) on the assumption that the P state is at zero potential. This suggests that the photoelectic disintegration mode is reasonably accurately known relative to the photomagnetic disintegration mode.

In (Ro67) the equations for the cross sections σ_m and σ_e are given which take into account the shape dependent term $-Pk^4r^3$. The review article on nucleon-nucleon effective range parameters (No72) points out that for nucleon-nucleon

scattering below 9.71 MeV in the laboratory system one can still use the shape independent correction (equ. 2.7) obtained from one pion exchange (OPE) models. At higher energies and for very accurate measurements the shape dependent terms are important. Furthermore both higher order terms shown in equ. 2.8 must be taken into account. The reason for this is that if the $-Pk^4r^3$ term alone is taken into account it depends significantly on the choice of a and r. There is also a strong correlation between P and Q (see equ. 2.8) and they might depend on a common parameter. The Cini-Fubini-Stanghellini approximation (Ci59) for $k\cot\delta_s$ which is also obtained for OPE models is suggested as a substitute to use in shape dependent calculations at higher energies.

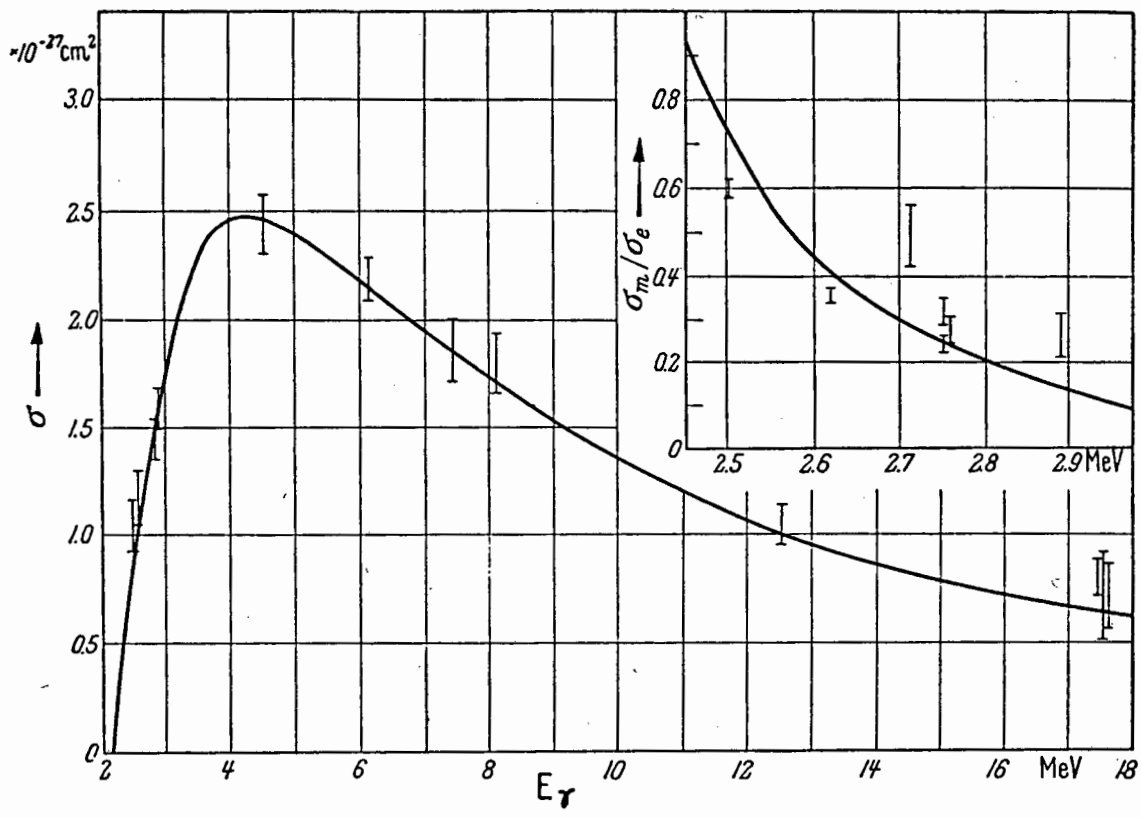

Figure 2.1 A plot of the cross section and the σ_m/σ_e ratio for deuteron photodisintegration versus incident photon energies. (Figure from (Hu57))

Because of Hulthen and Nagel (Hu53) confidence in the accuracy of the theory for the electric cross section it was hoped that an accurate measurement of the ratio σ_m/σ_e would supply an accurate value of σ_m as it is difficult to measure in scattering experiments. This was unfortunately only a hope as it was realized that there was uncertainty about the extent of the exchange currents which play a large role in the photmagnetic disintegration. If one looks at Fig. 2.1 then one can see that there is a good agreement with the data and that from here on accurate measurements and sophisticated theories are needed to explain the residual differences.

2.3 Semi phenomenological theories.

From photon absorption (electric or magnetic) in perturbation theory the transition probability per unit time also known as the "Golden Rule" is

$$\omega = \int \frac{2\pi}{\hbar} |T|^2 \rho(E) \, d\Omega \qquad 2.12$$

where $\rho(E)$ is the density of states at energy E of the particle, emerging in a solid angle $d\Omega$ and T the transition matrix for the transition. To convert the transition probability to cross section, ω must be divided by the flux c of incident particles per cm^2 and the photon density normalized to 1 per unit volume. The differential cross section is then

$$d\sigma/d\Omega = \frac{2\pi}{\hbar c} |T|^2 \rho(E) \qquad 2.13$$

The transition matrix T can be determined by evaluating non-relativistically the matrix elements of the interaction Hamiltonian H_{int} which describes the interaction of electromagnetic radiation with a system of nucleons. The

interaction Hamiltonian H_{int} is calculated as a first order perturbation of the eigenstates of the nuclear Hamiltonian H_o.

One of the improvements introduced calculations of the nuclear part of the Hamiltonian using potentials other than the more simple square well, exponential tail, gaussian and Yukawa potentials. Most of the new generation of semi phenomenological potentials have a similar form, (De84)

$$V = V_C + V_\sigma \sigma_1 \cdot \sigma_2 + V_T S_{12} + V_{SO} L.S + V_Q Q_{12} \qquad 2.14$$

where

V_C is the central component,

$V_\sigma \sigma_1 \cdot \sigma_2$ the spin dependent component,

$V_T S_{12}$ the tensor component,

$V_{SO} L.S$ the linear LS component and

$V_Q Q_{12}$ the quadratic spin-orbit component of the potential. The exact form of each of these components differ from potential to potential. A non relativistic reduction of the one pion exchange mechanism leads to a potential of this form.

For the bound state, potentials of this form lead to a coupled set of differential equations of the general form

$$\begin{aligned} u'' &= [\alpha^2 + U_{00}]\, u + U_{02} w \\ w'' &= [\alpha^2 + 6/r^2 + U_{22}]\, w + U_{20} u \end{aligned} \qquad 2.15$$

where u and w are the radial wave functions for S and D components respectively (Er84) and $U_{ij} = MV_{ij}$. It is the tensor part of the interaction (U_{02},U_{20}) that provides the binding as the central potential U_{00} is weak and the D state interaction U_{22} provides no binding.

The widely used Hamada-Johnston potential (Ha62) was used in the much quoted calculation for deuteron photodisintegration by Partovi (Pa64). The potential has a hard core and OPE tail that includes a tensor component which gives a 7% D state probability. It also had at the time the best fit to scattering data below 315 MeV but gives a singlet scattering length 40% smaller than measured values. Partovi's calculations were made for gamma energies ranging from 10 MeV to 140 MeV where the electric transitions are by far the strongest. The calculation also excludes explicit meson effects and multipoles higher than octupole. A criticism leveled at Partovi's calculations by Rustgi et al. (Ru83) is that use is made of the laboratory frame before and the centre-of-mass frame after the disintegration.

The Hamiltonian which describes the system (neglecting the free energy of the electromagnetic field) is given by

$$H = H_o + H_{int} \qquad 2.16$$

where

$$H_{int} = -\int \bar{J}(\bar{r}).\bar{A}(\bar{r})dr$$

with

$\bar{J}(\bar{r})$ = the current density operator and

$\bar{A}(\bar{r})$ = the vector potential operator for the electromagnetic field.

In the lowest order the current density operator for the two nucleon system $\bar{J}^{int}(\bar{\xi})$ can be written as the sum of the single particle current operators which may be split into an orbital convection current $\bar{J}^{c}(\bar{\xi})$ and spin current $\bar{J}^{s}(\bar{\xi})$.

$$\bar{J}^{int}(\bar{\xi}) = \bar{J}^{c}(\bar{\xi}) + \bar{J}^{s}(\bar{\xi}) \text{ with} \qquad 2.17$$

$$\bar{J}^c(\bar{\xi}) = \frac{1}{2M} \sum_{\alpha=1}^{2} [\zeta_\alpha(\bar{\xi})\ \bar{\pi}_\alpha + \bar{\pi}_\alpha\ \zeta_\alpha(\bar{\xi})] \quad \text{and}$$

$$\bar{J}^s(\bar{\xi}) = \frac{e}{2M} \sum_{\alpha=1}^{2} \bar{\nabla}_\xi \times \bar{M}_\alpha(\bar{\xi}) \qquad 2.18$$

where $\zeta_\alpha(\bar{\xi})$ is the charge density operator, $\bar{\pi}_\alpha$ the momentum operator and $\bar{M}_\alpha(\bar{\xi})$ the magnetization operator for nucleon (Pa64). Furthermore it is convenient to expand the vector potential

$$\bar{A}(\bar{r}) = \Omega_N^{-\frac{1}{2}} \sum_{\bar{w}} \sum_{\mu=\pm1} (2\pi/w)^{\frac{1}{2}} (a_{\bar{w}} \bar{\epsilon}_\mu e^{iw.\bar{x}} - a_{\bar{w}\mu}^{\dagger} \bar{\epsilon}_{-\mu} e^{-i\bar{w}.\bar{x}}) \qquad 2.19$$

in terms of electric and magnetic multipoles

$$\begin{aligned}
\bar{\epsilon}_\mu e^{i\bar{w}.\bar{\xi}} = \sum_{Lm} D^{(L)}_{m\mu}(0,-\theta,-\phi) \times \\
\{ -(\tfrac{2\pi(2L+1)}{L(L+1)})^{\frac{1}{2}} i^{L+1} \tfrac{1}{w} \bar{\nabla}_\xi (1+\xi\tfrac{d}{d\xi}) j_L(w\xi) Y^{(L)}_{(m)}(\theta,\phi) \\
-(\tfrac{2\pi(2L+1)}{L(L+1)})^{\frac{1}{2}} i^{L+1} w\bar{\xi}\ j_L(w\xi) Y^{(L)}_{(m)}(\theta,\phi) \\
-\mu(\tfrac{2\pi(2L+1)}{L(L+1)})^{\frac{1}{2}} i^{L} j_L(w\bar{\xi})[\bar{L}\, Y^{(L)}_{(m)}(\theta,\phi)]\}
\end{aligned} \qquad 2.20$$

where $D^{(L)}_{m\mu}(o,-\theta,-\phi)$ is the rotation function (see (Pa64)) and $Y^{(L)}_{(m)}(\theta,\phi)$ spherical harmonics. In equ. 2.19 $a_{\bar{w}\mu}$ is the annihilation operator for a photon of momentum $\bar{w}$ and polarization μ, and $\bar{\epsilon}_\mu$ are spherical unit vectors. The first two terms give rise to the electric multipoles and last term to the magnetic multipoles. In the long wavelength limit (e.g. for photons of low energy) the electric multipole contribution may be approximated by the first term. The sequence of these multipoles are E1, E2+M1, E3+M2,....

The wave functions used are the deuteron wave function for the initial state wave function and the n-p scattering wave function for the final state wave function.

The widely used Paris potential (La80) uses n-p scattering data in the energy range (laboratory frame) 13-350 Mev as well as p-p scattering data from 3-330 MeV

(laboratory frame). Although the data used do not extend down to the energy at which this experiment was done, the potential does include OPE. It also includes 2π and ω-exchange thereby giving a fairly realistic description of the long and medium range part of the NN force. Due to the uncertainty in the origin of the short range part of the NN force this part of the Paris potential is determined phenomenologicaly and has effectively a constant soft core. This potential is therefore good for use in the low and medium energy range. Another improvement was the inclusion of more transitions than the two used in the old analytical calculations. The first few allowed transitions are

$$E1_{ordinary} : ({}^3S_1 + {}^3D_1) \rightarrow {}^3P_0,\ {}^3P_1,\ ({}^3P_2 + {}^3F_2)$$

$$M1_{ordinary} : \rightarrow ({}^3S_1 + {}^3D_1),\ {}^3D_2$$

$$M1_{spin\text{-}flip} : \rightarrow {}^1S_0,\ {}^1D_2$$

$$E2_{ordinary} : \rightarrow ({}^3S_1 + {}^3D_1),\ {}^3D_2,\ ({}^3D_3 + {}^3G_3) \quad 2.21$$

The inclusion of higher multipoles and interference between the transitions add three extra terms in equ. 1.1 (De59)(Ru60). The differential cross section for the photodisintegration process is now given by

$$\sigma(\theta) = a + b\sin^2\theta \pm c\cos\theta \pm d\cos\theta\sin^2\theta + e\sin^2\theta\cos^2\theta \quad 2.22$$

for photoneutrons (-) and photoprotons (+) (Ru60). The higher order multipoles are not expected to play an important role at energies close to threshold although the E2 contribution could be important as pointed out by Holt (Ho81) from data down to E_γ = 3.5 MeV and supporting

calculations from Hadjimicheal (private communication). It would lead to an asymmetry in the angular distribution.

It is also in the interaction part of the Hamiltonian that the meson exchange effects are accommodated. The fact that the NN interaction is due to the exchange of mesons has been realized since the mid thirties but was not included into calculations because of the difficulties of handling large calculations before the advent of modern computers. Villars did however set out the various matrix elements of pion exchange operators in 1947 (Vi47) and these together with two other processes were used by Riska and Brown (Ri72) in explaining the longstanding 10% discrepancy between theory and data for n-p capture at threshold.

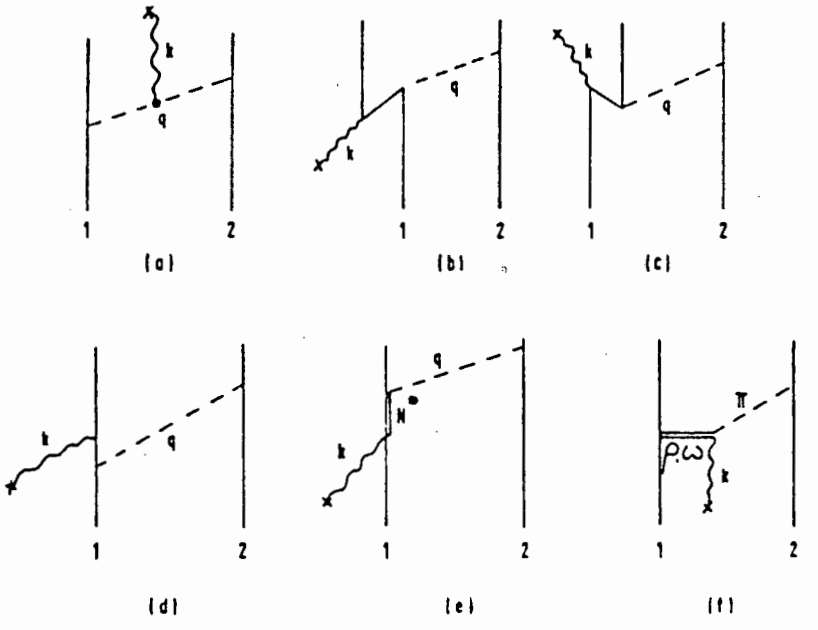

Figure 2.2 Time ordered Feynman diagrams of mesonic exchange processes which were included into deuteron photodisintegration calculations by Hadjimicheal (Ha73). The diagrams are of a) the pion current; b),c) and d) the pair excitation currents; e) the nucleonic current and f) the $\rho\pi\gamma$ and $\omega\pi\gamma$ current. (Figure from (Ha73))

Contrary to belief at that time it was found that the matrix element from the ^1S continuum to the ^3D state was

nearly as large as that of the transition to the ^3S state. Hadjimichael (Ha73) added these meson exchange current (see Fig. 2.2) corrections to the spin-flip M1 transitions ($^3S_1$ to $^1S_0$ and $^3D_1$ to $^1D_2$) in deuteron photodisintegration for photon energies between 5 and 22 MeV. The part of the two body operator which is due to meson exchange currents is given by (Ch71)

$$M = \tfrac{1}{2}\frac{e\hbar}{2mc}\{(\bar{\tau}\times\bar{\tau}_2)_z[(\bar{\sigma}_1+\bar{\sigma}_2)g_I + T_{12}^{(x)}g_{II}] + (\bar{\tau}_1-\bar{\tau}_2)_z[(\bar{\sigma}_1-\bar{\sigma}_2)h_I + T_{12}^{(-)}h_{II}] + (\bar{\tau}_1+\bar{\tau}_2)_z[(\bar{\sigma}_1+\bar{\sigma}_2)j_I + T_{12}^{(+)}j_{II}]\} \qquad 2.23$$

where g_I, g_{II}, h_I, h_{II}, j_I, and j_{II} are functions containing the radial dependence and $T_{12}^{(x)}$, $T_{12}^{(-)}$ and $T_{12}^{(+)}$ where $T_{12}^{o} = (\bar{\sigma}_1 o \bar{\sigma}_2).\bar{r}\bar{r} - \frac{1}{3}(\bar{\sigma}_1 o \bar{\sigma}_2)$ and where $o = x, -, +$ and $\bar{\sigma}_1$, $\bar{\sigma}_2$ and $\bar{\tau}_1$, $\bar{\tau}_2$ isoscalar and isospin operators respectively. The correction at 5 MeV amounted to between 4 and 12%.

In most of these calculations use is made of the Siegert theorem (Si35) which has been investigated in detail by Friar and Fallieros (Fr84). Siegert noted that the total internal current density must satisfy the differential charge conservation law.

$$\bar{\nabla}_\xi.\bar{J}_{int}(\bar{\xi}) + i[H_o, \zeta(\bar{\xi})] = 0 \qquad 2.24$$

The first term arising from the electric multipole expansion (equ. 2.20) may be calculated exactly for the total current operator using the above expression. Because in this term no

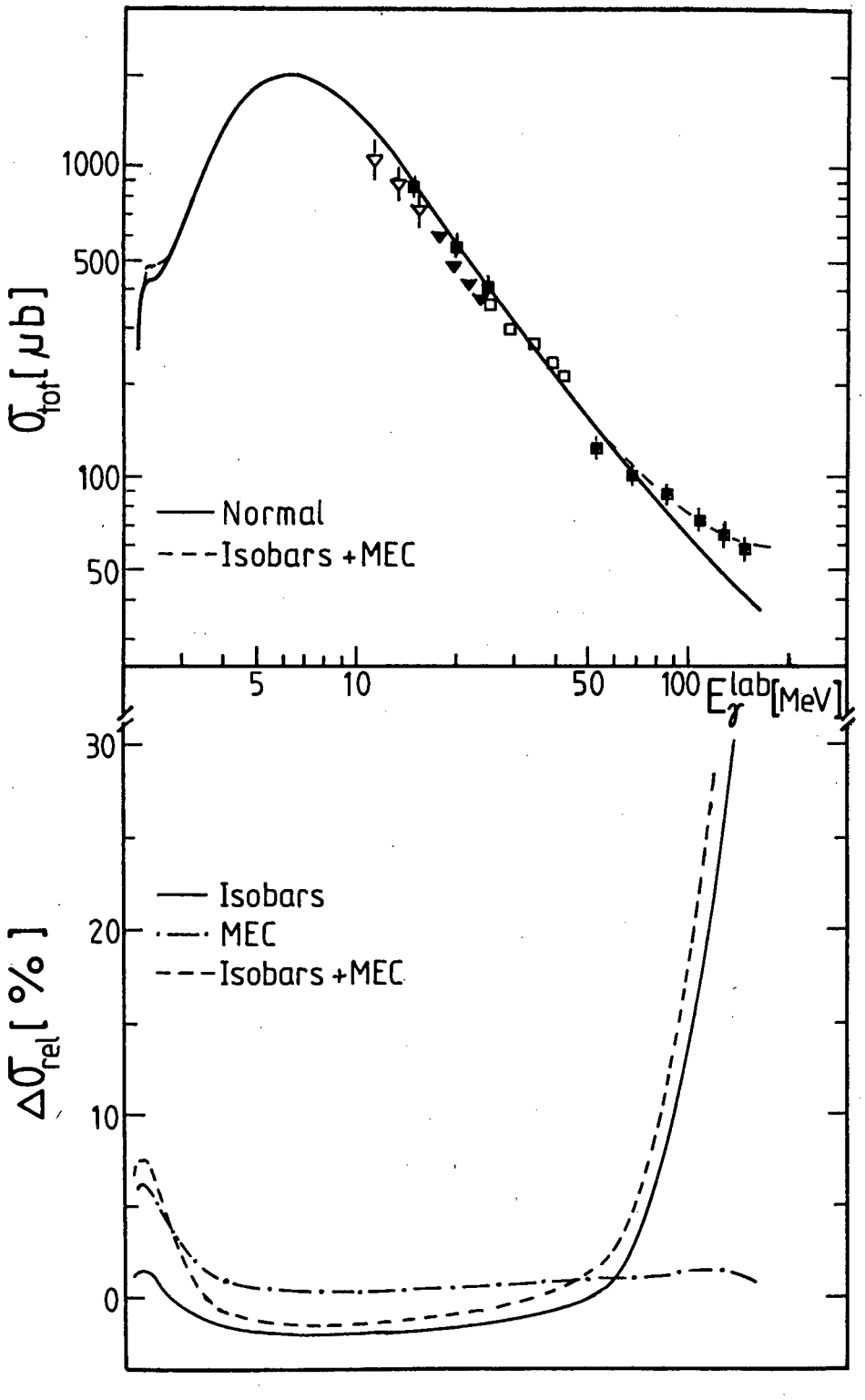

Figure 2.3 The total cross section for the deuteron photodisintegration reaction with and without interaction effects (upper part) and the relative contributions of MEC and IC (separately and combined) to the total cross section (lower part). Experimental data are from(Wh58), ∇; (Ba71), ▼; (We71), □ and (Al57), ■. Measurements at low energies do exsist but were not shown. (Figure from (Ar74))

approximation has been made in the form of the current operator, the effects of meson exchange currents are included even if one uses only single particle charge density operators, $\rho(\bar{\xi})$. At low photon energies the contribution to the transition matrix arising from this term includes meson exchange currents.

The Hamada-Johnston potential was also used by Arenhovel et al. (Ar74) for calculations in the region of threshold to 140 MeV. In addition admixture of explicit one pion exchange currents as well as NN(1470), NΔ(1236) and Δ(1236)Δ(1236) isobar configurations were used. Figure 2.3 taken from this paper shows that in the threshold region meson exchange current contributes up to 6% to the total cross section for the D(γ,n) reaction while isobar configurations contribute at most 1%. The meson exchange current correction effects only the magnetic transitions so that it is expected that the effect on the differential cross section may be as large as 20%.

In a later paper on neutron polarization in photodisintegration at low energies (Ru83a) the calculations are broadend to include the two body relativistic corrections to charge and current density calculated by Cambi et al. (Ca82). Rustgi et al.'s calculations were done with several potentials namely supersoft-core B and C, Paris, Hamada-Johnston and Yale for incident gamma energies from 6 to 14 MeV. All meson exchange currents used by Hadjimichael et al. (Ha73) as well as ρ- and ω- mesons were included. The best fit to polarization data (Ho83)(Na72) was given by

supersoft-core B without the two-body charge density effects.

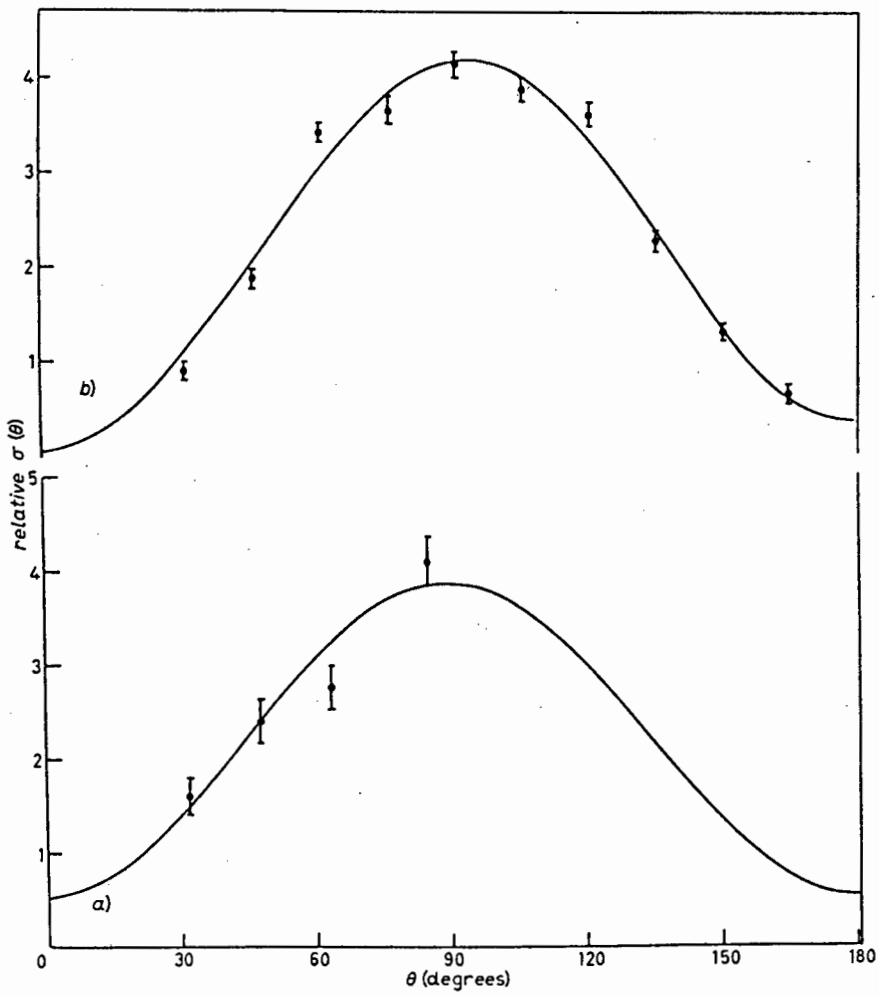

Figure 2.4 Relative differential cross sections for the deuteron photodisintegration reaction for gamma ray energies of a) 2.72 MeV (data from (Wo49)) and b) 9.0 MeV (data from (Bö63)) and curves from (Ru83) using a Yale potential. (Figure from (Ru83))

In another paper by Rustgi et al. (Ru83) where the effects of electromagnetic retardation in the D(γ,n) reaction are investigated a fit of the angular distribution data of Woodward and Halpern (Wo49) at 2.72 MeV and Bösch et al. (Bö63) at 9.0 MeV is shown (see Fig. 2.4). Unfortunately no values of the parameters a, b, c, d and e are given. Values for these parameters are given in the paper of Rustgi et al. (Ru84) but only down to 4.0 MeV. This highlights the

problem in the energy region just above threshold in that there are no explicit calculations of differential cross sections which include meson exchange currents.

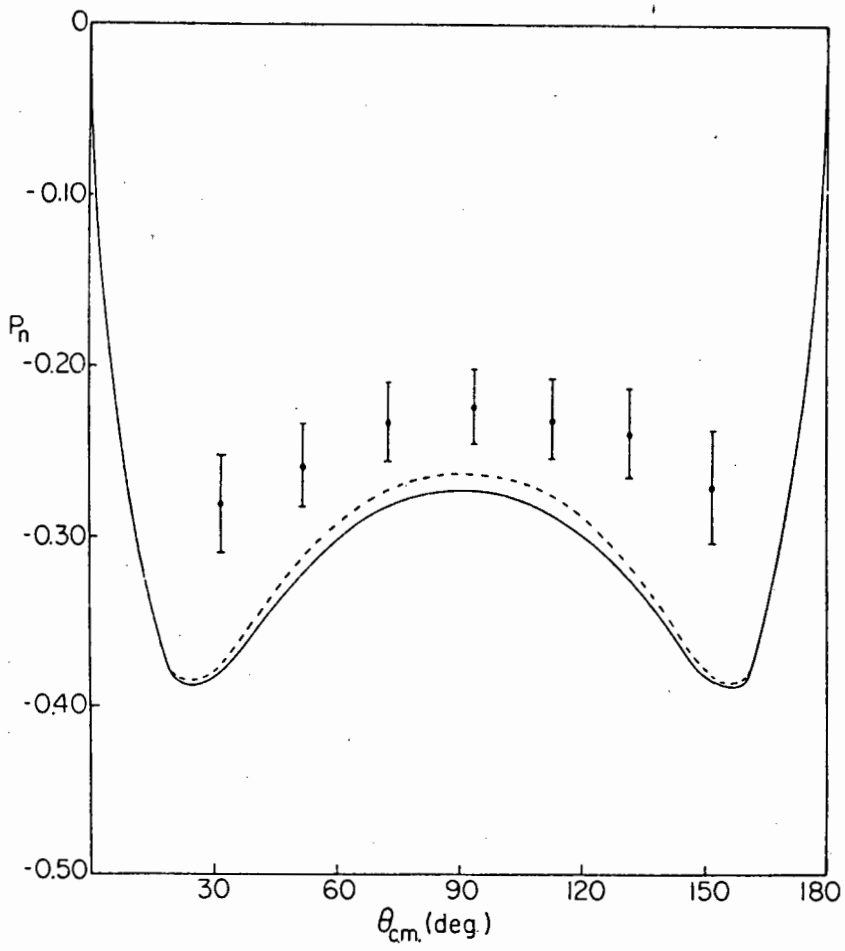

Figure 2.5 The polarization data of Jewell et al. (Je65) compared to calculations by (Ru84) for a SSC-B potential with (solid curve) and without (dashed curve) two-body charge and current effects.(Figure from (Ru83a))

If one looks at the fit of theoretical curves by Rustgi et al. (Ru83a) to the polarization data of Jewell et al. (Je65) (see Fig. 2.5) at 2.75 MeV then the ~18% discrepancy points to a still serious deficiency of theory in this energy region. This was pointed out by Cameron (Ca84) at a recent conference on photonuclear work in Canada.

It seems that as more is learnt and understood about the internal structure of nucleons the better the NN force

is understood and can be described. The good agreement between theory and (a controversial choice (Ar81) of) data achieved by Hadjimicheal and Saylor (Ha80) at higher energies with explicit introduction of quarks might be the signpost of things to come.

CHAPTER 3

The Experiments

3.1 Introduction.

The dipole cross section ratio σ_m/σ_e is expected to be sensitive to meson exchange current effects at energies close to threshold through the M1 component which dominates other components only in this energy region.

For this reason the initial interest in this project was focused on the $^{14}N(p,p'\gamma)$ reaction as a source because of its strong 2.313 MeV gamma, only 88 keV above the $D(\gamma,n)p$ threshold. This energy is lower than energies at which similar measurements were made. The σ_m/σ_e ratio is therefore correspondingly higher, making it particularly attractive. This work (described in section 3.2) was done at the VDG Group NAC* which will be referred to from here on as the VDG. The neutron background problems associated with this reaction led to the use of neutron radiation free radioactive sources.

Preliminary experiments with Th, ^{72}Ga and ^{24}Na sources (described in section 3.3) were done at the UCT+, Pelindaba (AEC)$ and the VDG. The final experiments (described in section 3.4) were carried out at the VDG. The VDG proved a most suitable venue for this work for two reasons. Firstly, ^{24}Na sources of quite adequate strengths could be produced continuously by the accelerator, as described in section 3.4.2. Secondly, the VDG multiparameter data acquisition system (described in section 3.4.5) could be used, allowing a five parameter experiment to be undertaken.

* National Accelerator Centre
\+ University of Cape Town
$ Atomic Energy Corporation

These final experiments have several important features (described in section 3.4.1) which differ from previously published experiments such as the detection of both photoproducts, the measurements at forward as well as backward angles and an in situ efficiency calibration of the photoneutron detector. The experimental geometry, electronic circuit and neutron efficiency calibration are described in sections 3.4.2, 3.4.3 and 3.4.4 respectively.

3.2. The Early Work.

To start with a search was made to find reactions which produce gamma rays in the threshold region (2.23 - 2.8 MeV) of sufficient intensity to be used as a source for $D(\gamma,n)$ measurements. Although there are several reactions with suitable gamma rays, it is difficult to find one with a yield large enough to compensate for the low cross section in the threshold region of the $D(\gamma,n)$ reaction. The most suitable found was the $^{14}N(p,p'\gamma)$ reaction in which the 2.313 MeV first excited state state of ^{14}N may be strongly excited at incident proton energies below the $^{14}N(p,n)$ threshold (5.93 MeV).

The first attempts at measuring an angular distribution measurement for the $D(\gamma,n)$ reaction were thus made using this reaction as a source. A pulsed proton beam of 5.2 MeV from the Van de Graaff accelerator at the VDG was used on a nitrogen gas cell to excite the 3.95 MeV resonance in the $^{14}N(p,p'\gamma)$ reaction. This in turn produced an intense monoenergetic 2.313 MeV pulsed gamma source with no other gamma of any significance above the $D(\gamma,n)$ threshold.

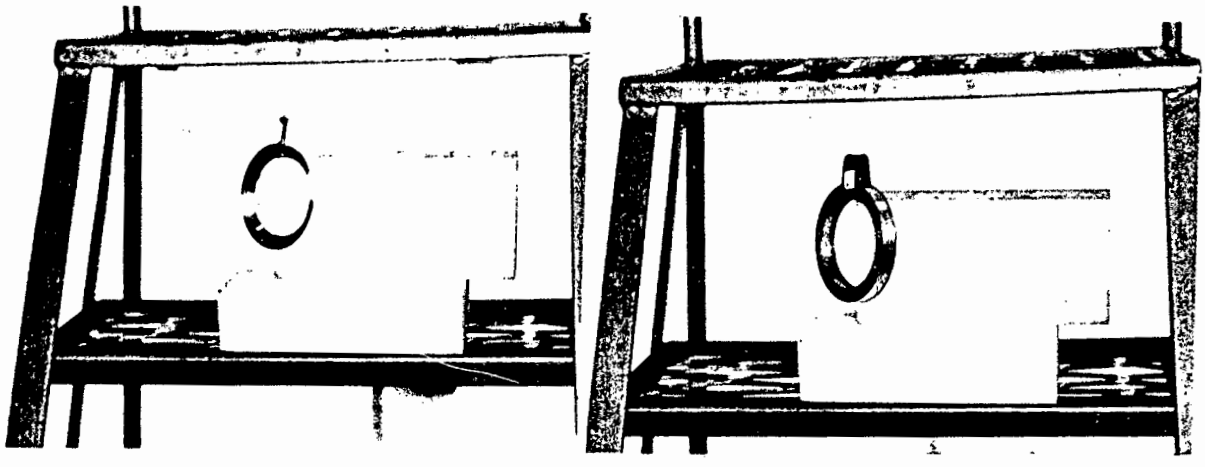

Figure 3.1 The toroids used in the early experiments were a thin angled one (left) and a thick one (right) with a square cross section.

The choice of a gas target was determined by the need to use high proton currents (>1 μA) and to avoid introducing elements which might contribute neutron background via (p,n) reactions. The gas cell had a thin platinum window and a platinum beam stop and its inner walls were lined with tantalum to minimize the neutron background from scattered protons. To increase the photoneutron signal, a toroid of D_2O was used as the target. Two toroids (see Fig. 3.1) were tried : firstly a thick toroid, 10 cm in diameter with a square cross section of 1 cm^2, and 1 mm thick aluminium walls; secondly a thin toroid of 2 mm thickness and a 1 cm width. The thin section of the toroid was angled at 45^o to the 8 cm diameter and its brass walls were 0.5 mm thick. Identical rings filled with H_2O were used for background runs.

The choice of neutron detector fell on a NE905 Li glass scintillator. Although this detector had no pulse shape discrimination (PSD) capabilities to discriminate against the high gamma flux it was found to be less sensitive than the proton recoil detectors, to the many high energy

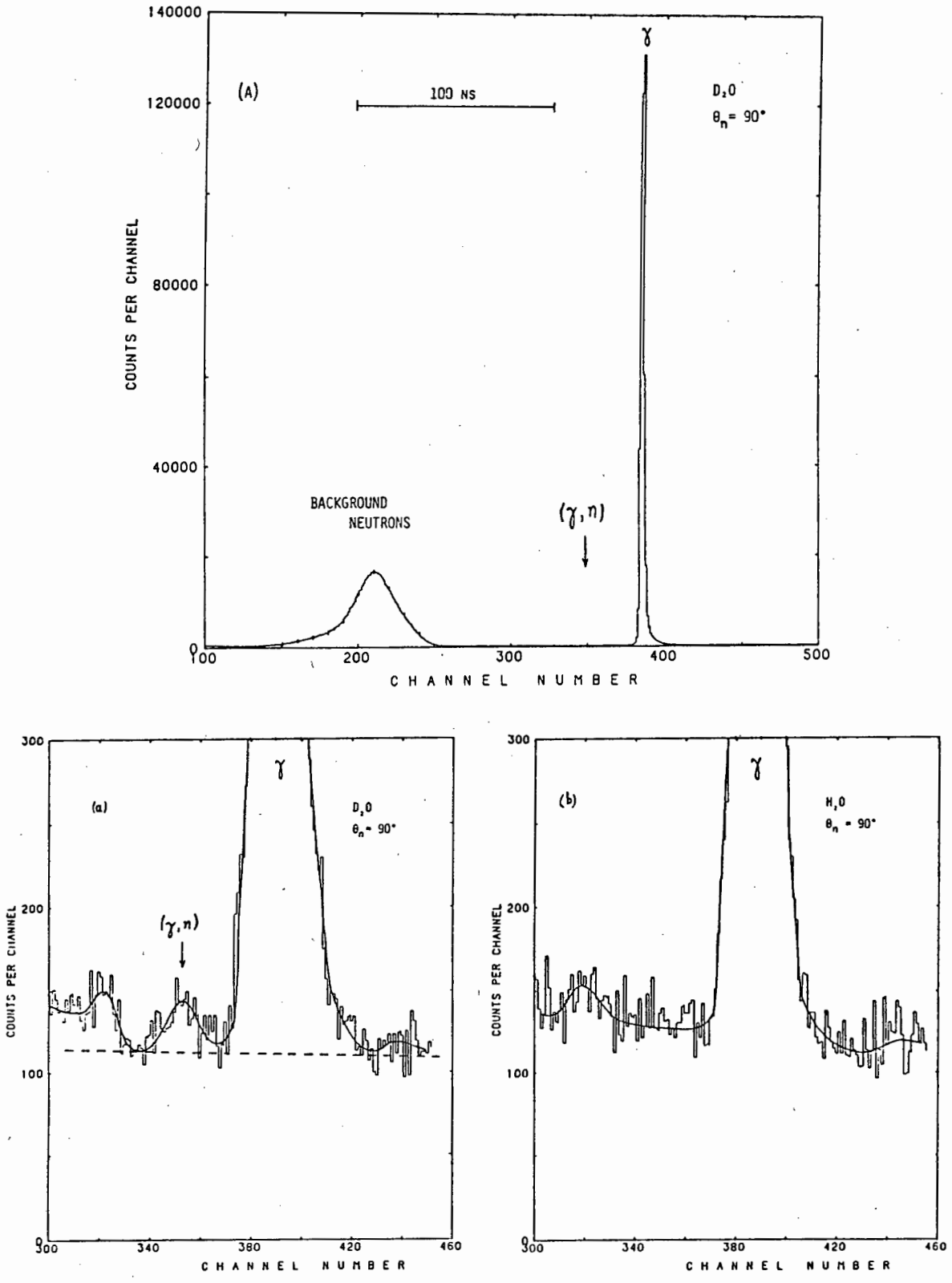

Figure 3.2 A pair of time-of-flight spectra for D_2O (bottom left) and H_2O (bottom right) samples showing the separated photoneutron peak on a rare occasion of the gamma peak having no tail. The upper frame, of which the bottom left frame is a portion, shows the size of the gamma peak and background neutrons. These spectra are both for 24 hour runs.

background neutrons from the beamline collimators, cell window and stop material. This proved to be the problem with the detectors tried which have PSD characteristics such as the NE213 and boron-loaded liquid.

Time-of-flight was used to separate the photoneutrons from the gammas. The small photoneutron peak was expected between the gammas and the background neutrons in the time spectrum (see Fig. 3.2) but the pulsed gamma peak had a tail on the trailing edge which swamped the small neutron peak unlike the one occasion shown in Fig. 3.2 when this was not the case.

3.3 Preliminary experiments with radioactive sources.

The neutron background in the accelerator experiments described above highlighted the major disadvantage of accelerator sources for this work and forced a return to radioactive sources which are free of this problem. The sources investigated with gamma rays in the energy region of interest were natural thorium (2.61 MeV $T_{1/2}$ = 1.41X10^{10} y), ^{72}Ga (2.51 MeV $T_{1/2}$ = 14.1 h) and ^{24}Na (2.75 MeV $T_{1/2}$ = 15.0 h) (Re83). The former because of its long half life was tried first, in the form of two cylindrical samples of natural thorium with a diameter and height of 2.54 cm.

The experimental arrangement used a deuterated anthracene crystal, mounted with the use of a light pipe, and functioning simultaneously as target and photoproton detector. A thick (7.5 cm) NE213 was used as the photoneutron detector in a time of flight set up. The two other parameters used in this experiment were the pulse heights of the NE213 and the deuterated anthracene detector.

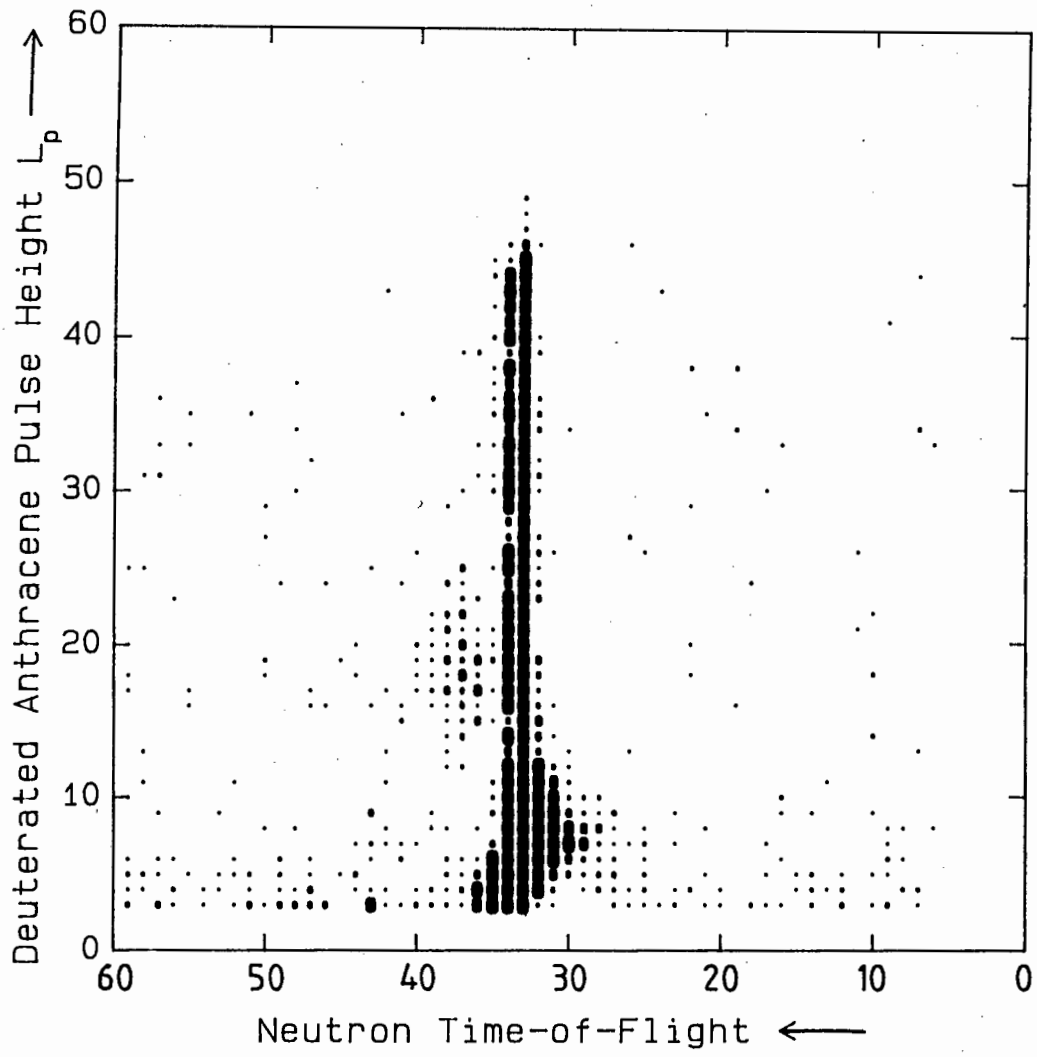

Figure 3.3 A density plot of counts versus deuterated anthracene pulse height, L_p, and neutron time-of-flight. The clear photoneutron signal from the D(γ,n) reaction using a Th source can be seen centred around position (38,18) to the left of the gamma locus.

This arrangement gave a clear photoneutron signature and proved the viability of the source experiments (Fig. 3.3).

Stronger sources were needed so the first gallium and sodium experiments were performed at Pelindaba in Pretoria where strong sources were produced using neutron activation in the Safari reactor.

The experiment was set up in the target area of the 3.75 MV Van de Graaff at Pelindaba. This made it possible to calibrate the photoneutron detector for relative neutron detection efficiency for the range of energies detected in the photodisintegration measurements without dismantling or even altering the settings for the photodisintegration experiment. The calibration was therefore effectively done in situ using monoenergetic neutrons obtained from the $^{7}Li(p,n)^{7}Be$ reaction. The experimental geometry was the same as used for the thorium source experiments apart from the addition of a GeLi detector to monitor the gamma flux.

As only a two parameter data acquisition system was available at Pelindaba, only the time of flight and the deuterated anthracene pulse height were recorded in these experiments. Both particle detectors made effective use of Link Model 5010 pulse shape discriminators (Ad78) with the busy signals from these Link units used in monitoring the detector dead times.

The neutron detection efficiency of proton recoil scintillation detectors is sensitive to the PSD setting used and cannot be determined accurately (<10%) from calculation at low (<0.3 MeV) energies. It is therefore necessary to make a careful measurement of the relative neutron detection

efficiency for the energy range of neutrons detected and with the same PSD settings used in the experiments. For this the NE213 was compared to a lithium glass scintillator which is insensitive to the bias setting at these neutron energies. The $^{7}Li(p,n)$ reaction was used to produce monoenergetic neutrons.

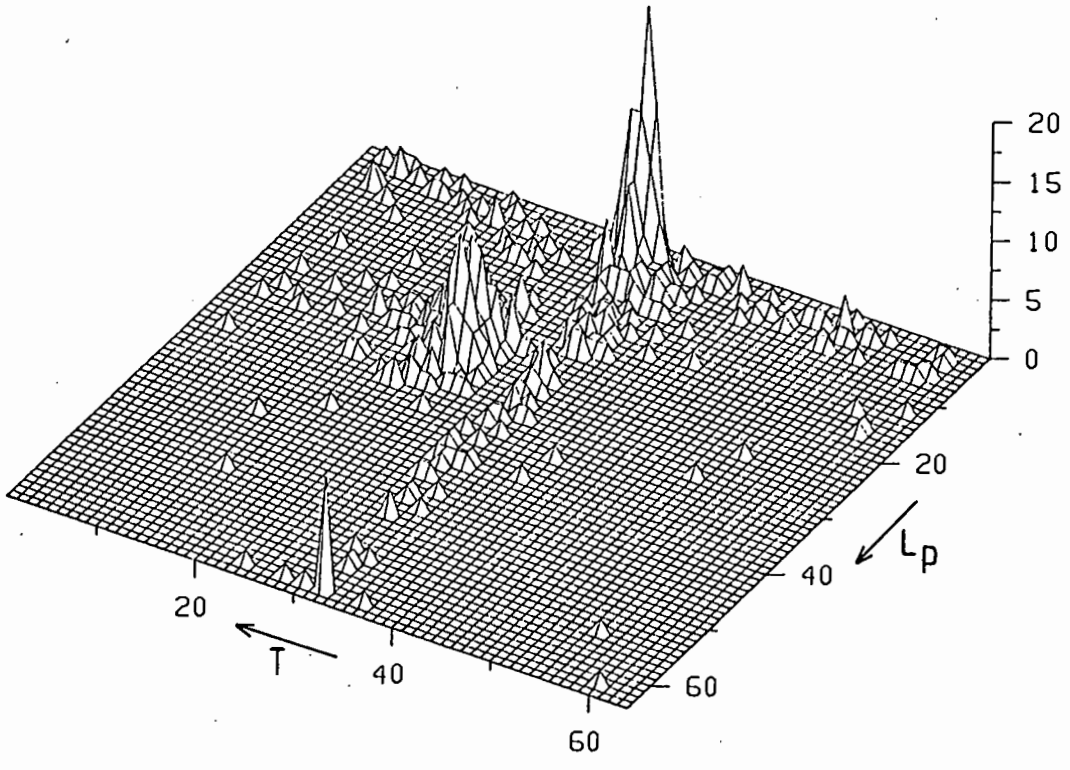

Figure 3.4 A perspective view of a plot of counts versus photoproton pulse height Lp and neutron time-of-flight showing the clear photoneutron signature on the left of the gamma locus with a low accidental background from the ^{24}Na source.

The ^{72}Ga has the lowest energy of the three sources considered and this made the photoneutrons more difficult to separate from the low pulse height background at small angles. A feature of this source is the high rate of low energy gamma rays emanating from it. The low energy component from the ^{24}Na source is very much smaller. Low energy gammas have a greater chance of breaking through the

PSD and lead to a significantly larger accidental coincidence background for measurements with ^{72}Ga sources as compared with ^{24}Na. In Fig. 3.4 a spectrum of photoproton pulse height versus neutron time of flight for ^{24}Na shows the low accidental background.

On the strength of these experiments and because of the long counting time required and because sodium had the most convenient characteristics of the three sources, it was decided to concentrate on sodium only in order to be able to make an accurate measurement.

These preliminary experiments also brought a number of problems to light. They indicated that the number of inscattered photoneutrons from the light pipe was significant. The broadening of the photoneutron peak in the time of flight spectrum due to the thick NE213 made it impossible to separate these inscattered photoneutrons from the direct photoneutrons. It was also demonstrated that the TAC contributed significantly to the dead time of the system.

Most importantly, the experiments showed that acquiring data with only two parameters was not flexible enough for this experiment. It was clear that at least five parameters needed to be recorded in order to ensure that all the necessary discrimination thresholds and windows could be optimally set during subsequent offline analysis, and also to ensure the backgrounds could be estimated reliably and simply. Multiparameter facilities were unfortunately not available at the Pelindaba Van de Graaff at that stage.

Interest then reverted to the feasibility of source experiments in Cape Town. It proved impossible to acquire a sufficiently strong ^{228}Th source. The feasibility of producing ^{24}Na via the $^{23}Na(d,p)^{24}Na$ reaction on the Van de Graaff was then investigated and it was found that sources suitable for this experiment could be produced quite readily.

3.4 The Final Experiments using ^{24}Na sources.

3.4.1 Introduction.

The final experiments consisted of three sets of runs, namely September 1984, November 1984 and February 1985. These experiments were completely dismantled between runs thus eliminating possible systematic errors in electronic "tuning" as pointed out by Weissman and Schultz (We71). The November data had better statistics than the September data. The February run was done with higher live time rates and larger inter detector distances in order to check the validity of the live time correction procedures.

Each set consisted of a number of 12 hour runs at different angles on a rotation basis to minimize systematic errors such as electronic drifts. Apart from the photodisintegration data each set also included a subset of neutron detector efficiency calibration runs and a number of calibrations and checks using radioactive sources.

A schematic overview of how the facilities at the VDG were utilized for the different running modes in the experiment can be seen in Fig. 3.5. In the "normal" mode the Van de Graaff was used to activate a sodium source via the $^{23}Na(d,p)$ reaction in a well-shielded target room (Fig. 3.5

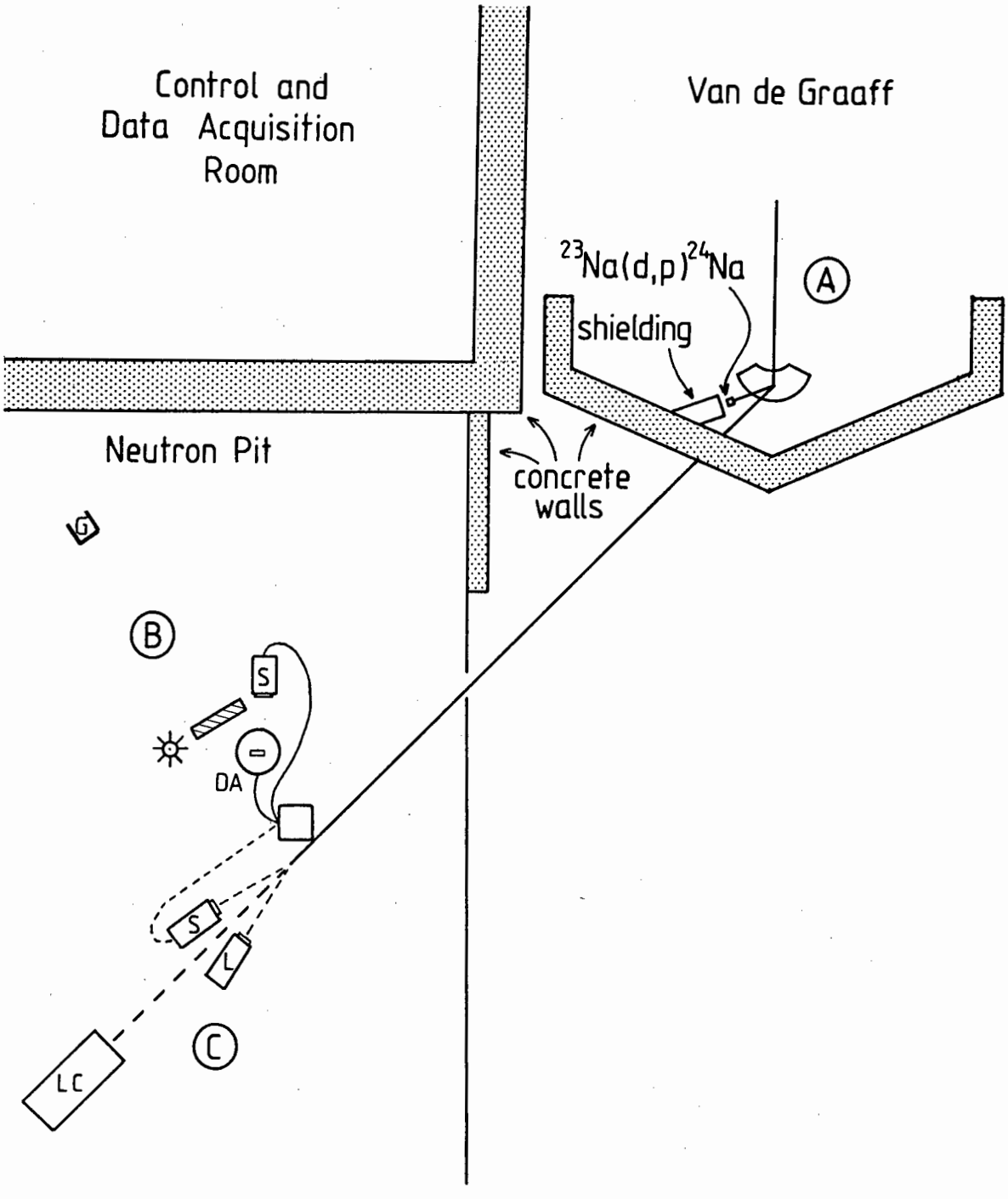

Figure 3.5 An overview of the experimental area of the VDG indicating the locations of the source activation (A), the photoneutron experiment (B), and the stilbene efficiency calibration (C),relative to one another. The neutron pit floor level is 2 m below the other floor levels and thereby provided further shielding for photodisintegration experiment from the source being activated. The photodisintegration experiment was situated on a 1 m high table in the pit. The shielding indicated consisted of borated wax-, lead- and concrete blocks.

section A) while the photodisintegration experiment ran simultaneously in a separate area (Fig. 3.5 section B) close to an unused beamline. The Van de Graaff supplied a fresh ^{24}Na source every twelve hours in this mode. In the "calibration" mode protons were delivered to a ^{7}Li target (Fig. 3.5 section C) close to the photodisintegration experiment and the resulting neutrons were used to calibrate the neutron detector used in the experiment.

This final experiment therefore included a number of important features namely;

1. Both photoprotons and photoneutrons were detected.
2. Measurements were made at forward as well as backward angles.
3. The 2.75 MeV gamma flux was monitored with a high resolution GeLi spectrometer.
4. Both photoproduct detectors had PSD capabilities to reduce the gamma background.
5. Time-of-flight was used to separate the true photoneutrons, which travelled directly to the detector, from those whose paths included one or more scatterings on outside components of the apparatus.
6. A Monte Carlo simulation for multiple scattering in the deuterated anthracene target was used to calculate a correction for these scattered neutrons, not eliminated by 5.
7. The relative efficiency of the neutron detector,as a function of neutron energy was calibrated effectively <u>in situ</u>, in an adjacent and auxiliary experiment using monoenergetic neutrons from the $^{7}Li(p,n)^{7}Be$ reaction.

8. Live times were carefully monitored in both the photoneutron and gamma spectrum measurements.

9. The multiparameter data acquisition system together with offline analysis made it possible to select optimal values for the various detection thresholds and discrimination windows used in both the photoproton and photoneutron detectors. It also enabled one to determine the final backgrounds reliably and without difficulty.

10. Several sets of independent measurements (4 exploratory and 3 final series of runs) were made in order to monitor the consistency of the results.

The merit of the experiment depends greatly on these features to reduce, eliminate and correct for some of the problems experienced in previously published measurements.

3.4.2 The Gamma Source.

A 5 MeV deuteron beam was used to activate natural sodium in sodium metaborate to ^{24}Na. The source consisted of fused sodium metaborate in a carbon crucible. These sources could be between 4 mCi and 8 mCi depending on beam conditions and irradiation time. Two sources were used which were alternately irradiated and used in the experiment for 12 hours because of their short half life. The quality of the source can be judged from the clean gamma spectrum in Fig. 3.6.

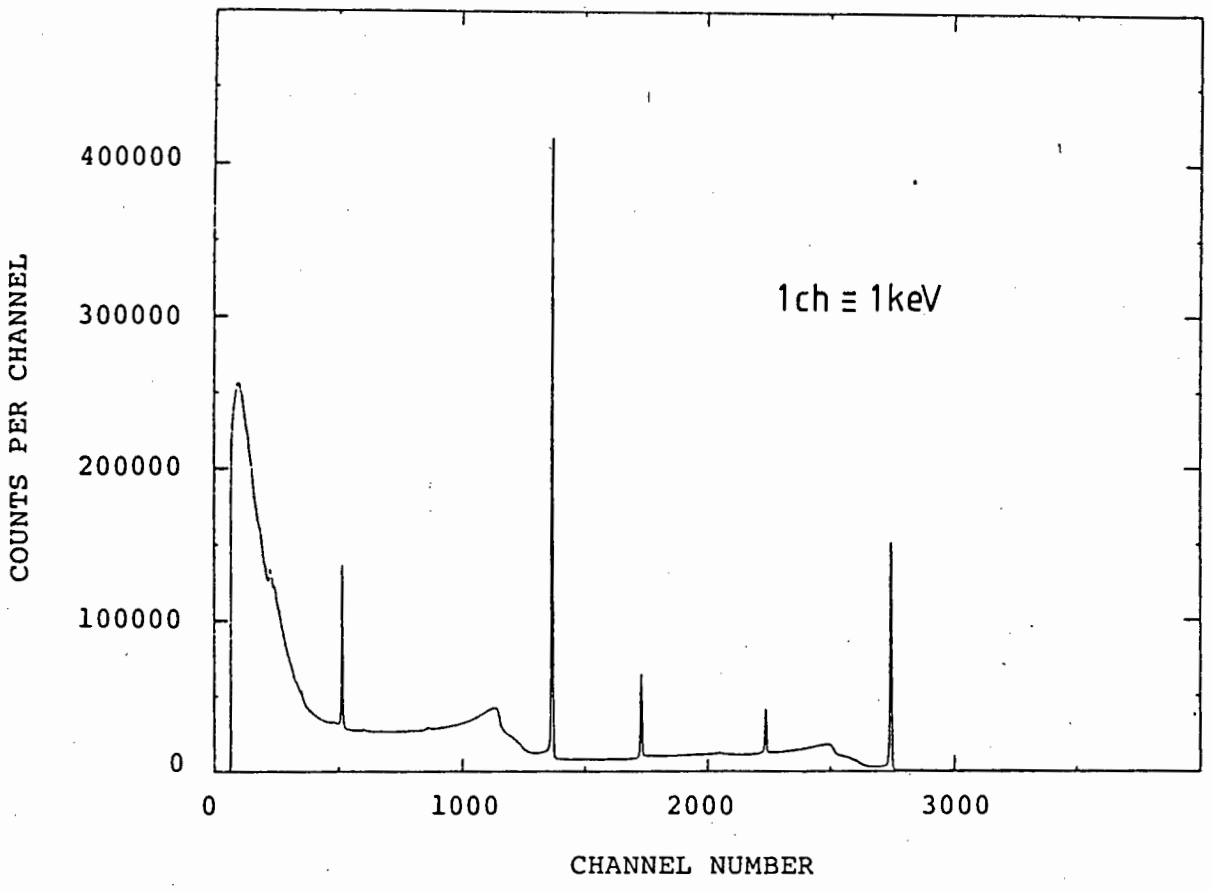

Figure 3.6 A GeLi spectrum of the 24Na gamma source used in the photodisintegration experiments.

3.4.3 The Gamma Monitor.

The 4K gamma spectrum from the GeLi, used as a monitor of the gamma flux incident on the deuterated anthracene crystal (DA), was recorded for each run. The GeLi was placed some 4.2 metres away from the source in order to limit electronic dead time in ADC 0 (Fig. 3.7) to < 10%. In addition to this the operating threshold of the gamma ADC was brought up to just below the 1.36 MeV peak in the ^{24}Na spectrum. Counts within a tight TSCA window set on the 2.75 MeV gamma peak were sent to a scaler providing an additional monitor of the gamma flux.

Table 3.1 Angle and distance measurements for the three series of final runs

Angles for all series		Distances for each series (see Fig. 3.7)			
Laboratory angle (deg.)	Centre of mass angle (deg.)	Run Series	source to DA (cm)	DA to Stilbene (cm)	DA to GeLi (m)
30.0	30.07	September	18.0	15.0	4.29
45.0	45.10				
60.0	60.13	November	18.0	15.0	4.29
90.0	90.16				
120.0	120.15	February	26.0	17.0	4.25
135.0	135.12				

After each run both the 1.36 MeV and 2.75 MeV peaks were recorded and integrated (which included a background correction) online. The arm on which the source was mounted could be adjusted for different source-to-DA distances as well as for different γ-n angles θ_L (see Fig. 3.7). Table 3.1 shows the different distances used in the three different data series.

3.4.4 The Geometry.

The geometry used in these experiments is schematically represented in Fig. 3.7. A 1 cm diam. x 2 cm long deuterated anthracene crystal (DA) was used as a target and detector of photoprotons. Because the dimensions of the crystal are large relative to the range of the photoprotons the detection efficiency for the photoprotons is almost 100%.

A further advantage of the crystal is its anisotropic scintillation response. The c' axis of the crystal along which there is an enhanced pulse height (Br74a) was set in the direction of the neutron detector. The pulse height of the recoiling photoprotons associated with the chosen neutron direction are enhanced by this effect (see Fig. 4.2). The crystal has good PSD properties which were also used.

The light pipe used in the preliminary runs was abandoned in order to eliminate in-scattering of photoneutrons from this source. The crystal was suspended, with the aid of thin cotton threads, between two photomultiplier (RCA 8850) tubes for good light collection. The tube faces were 4cm away from the center of the crystal.

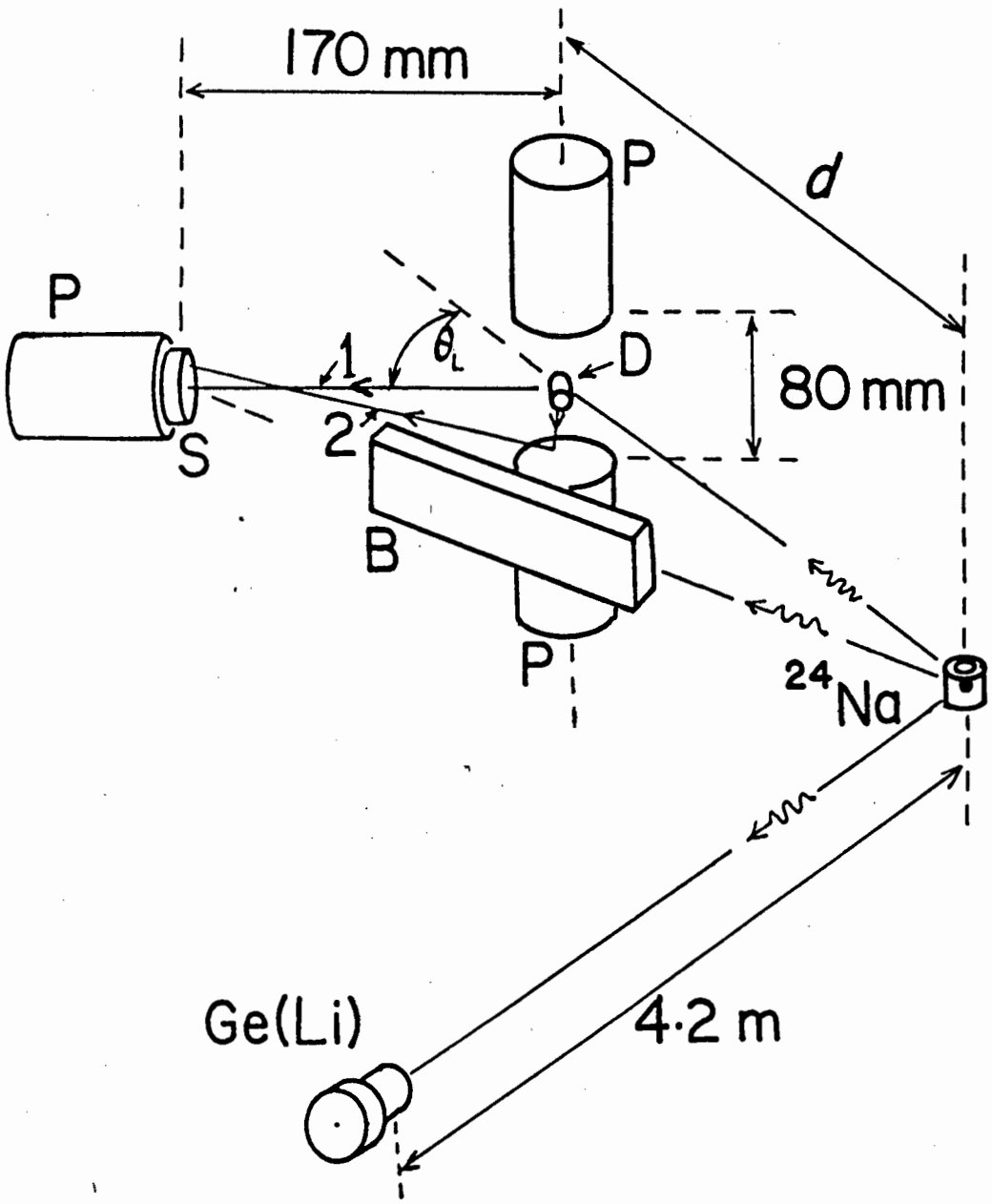

Figure 3.7 The geometry used for the photodisintegration experiments. Here D is the deuterated anthracene crystal, S, the stilbene crystal, B, hevimet shielding, P, the photomultiplier tubes, and 1 and 2 showing the pathlengths of direct photoneutrons and inscattered photoneutrons off a photomultiplier tube face respectively.

Time-of-flight was then able to separate direct photoneutrons (path 1 in Fig. 3.7) from any photoneutrons scattering off the photomultiplier tube faces (path 2 in Fig. 3.7) into the photoneutron detector.

The photoneutron detector used was a stilbene crystal (5.0 mm radius and 20.0 mm long) mounted on the photomultiplier (RCA 8575) face. The PSD properties of this crystal (see Fig. 4.2) were similarly used to discriminate against the high gamma ray flux. A hevimet shadow shield was used to attenuate gammas travelling directly from the ^{24}Na source to the stilbene crystal. Care was taken not to put the shield too close to either detector, so that inscattered photoneutrons from this source would still be separated by time-of-flight.

3.4.5 The electronic circuit.

Figure 3.8 is a block diagram of the electronic circuit used with the geometric setup described above (Fig. 3.7). The five parameters recorded for each accepted event were the pulse heights (marked L_p and L_n) from the two detectors, the short pulse integrals (marked F_p and F_n) from the respective Link units (see below) and the time-of-flight between the two detectors marked T. The p and n subscripts denote the type of photoproduct being detected.

These five parameters were acquired in a coincidence geometry. The coincidence requirement reduced the amount of accidental background accepted and so helped increase the signal to background ratio.

To explain what is meant by the short pulse integral it is necessary to go to the basic idea used in PSD. This is

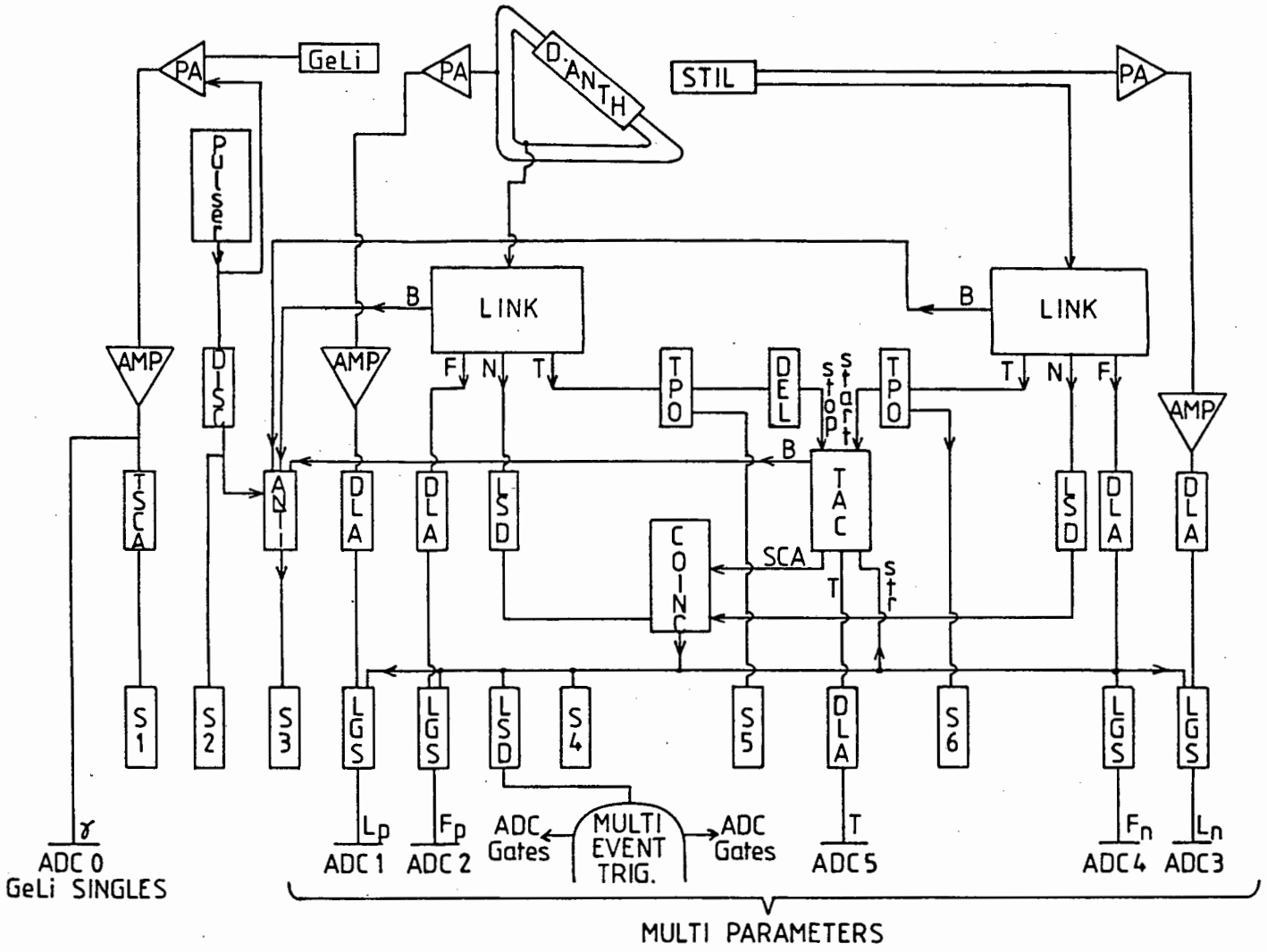

Key to abreviations

AMP	:	Amplifier
ANTI	:	Anticoincidence
B	:	Busy output
COINC	:	Coincidence
DEL	:	Delay
DLA	:	Delay amp
DISC	:	Integral discriminator
F	:	Short integral output
F_p, F_n	:	Fast integral signals
LGS	:	Linear gate and Stretcher
LINK	:	Link PSD unit
L_p, L_n	:	Pulse height signals
LSD	:	Logic shaper and delay
N	:	Neutron output
PA	:	Preamp
S1-S6	:	Scalers
SCA	:	Single channel analyser
Str	:	Strobe input
T	:	Timing output
T(ADC5)	:	Time-of-flight signal
TAC	:	Time-to-amplitude convertor
TPO	:	Time pick-off
TSCA	:	Timing single channel analyzer

Fig 3.8 A schematic representation of the electronic circuit used in the final photodisintegration experiments.

namely that in scintillators with PSD properties, scintillations have a fast (a few nanoseconds) and slow (a few hundred nanoseconds) component, and while most of the light comes in from the fast component, the amount of slow component varies with the type of particle causing the scintillation. A gamma ray causes a smaller slow component than a neutron which in turn is less than that of a deuteron. In fact the heavier the particle being detected the larger the the slow component. PSD compares the ratio of fast to slow components to differentiate between particles.

The method of operation used by the LINK PSD unit (Ad78) consists of taking an integral over a period comparable to that of the fast component of the scintillator and comparing it with the integral of the first 400 nsec of the scintillation pulse being detected. The pulse shape parameter is then proportional to the difference between the long and short integrals. The unit has a logic output for every event passing the criteria designating it as a neutron.

Unfortunately the only shape output from these units are designed for driving oscilloscope displays and not for ADC interfacing. A modification was therefore made to these units to extract the short integrals F_p and F_n to facilitate the generation of software pulse shape parameters S_p and S_n respectively. The offline generation of these pulse shape parameters is explained in the next chapter.

The high gamma flux in which the experiment needs to run necessitates that the live time be very carefully monitored. This was done by taking the busy signals from the

TAC and the two LINK modules in anticoincidence with the pulser as shown in the block diagram of the circuit (Fig. 3.8). The ratio between the scaler from the coincidence unit and the scaler from the pulser is then the fraction of time for which the system is live. The TAC had by far the greatest influence on the live time of the system.

The live time of the separate singles gamma ADC was monitored by sending the pulser into the test input of the GeLi preamplifier. This was done for the last two runs in the set of three used. The lack of a gamma live time correction for the Feb. data series should have an estimated effect of less than 1% on the result for this series.

To monitor the stability of the detectors and electronics, source calibrations were done at the beginning middle and end of the experiments. An ^{241}Am source was used to check both the LINK units cutoffs and gains relative to the position of the 60 keV peak. To check the coincidence timing of the circuit a ^{22}Na source was used.

3.4.6 The Neutron Efficiency Calibration.

The energy of the photoneutrons varies with the angle of emission relative to the direction of the incoming gamma rays. This kinematic spread makes it necessary to determine the relative detection efficiency of the photoneutron detector as a function of neutron energy. The relationship between the photoneutron energy E_n and the angle θ_L in the laboratory frame was derived from

$$E_\gamma = \frac{(M_p - M_n - M_d) + 2M_d(E_n + M_n)}{2[2M_d - (E_n + M_n) + 2((E_n + M_n) - M_n\cos\theta_L)]} \qquad (3.1)$$

given by (Sh70).

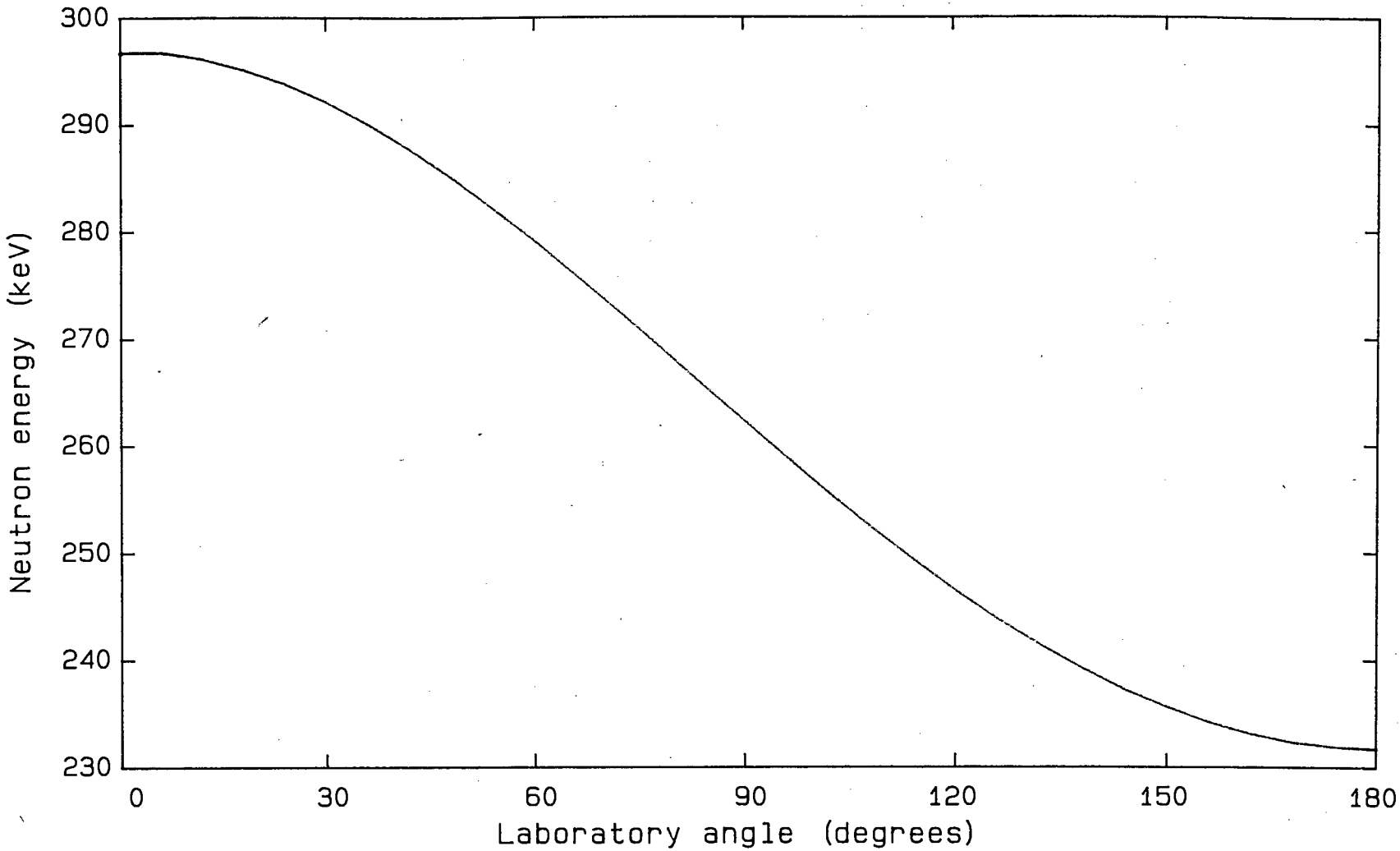

Figure 3.9 Plot of the photoneutron energy versus θ_L, the angle of emission in the laboratory frame.

The variation of E_n for photodisintegration by 2.75 MeV gammas can be seen in Fig. 3.9. The difference in angle between centre-of-mass angles, θ, and laboratory angles, θ_L, can be seen in Table 3.1 and is negligably small so that angles will be referred to as θ from here on. The energy variation with angle for the photoproton detector is of no consequence because of the ~100% detection efficiency of this detector for all energies.

The system efficiency of the system as a neutron detector is sensitive to the PSD settings on the LINK module of the stilbene scintillators. It is therefore necessary to calibrate this system under the exact conditions used in the "normal" mode of the experiment. The detector was therefore lifted from its position in the experiment and moved to its position for calibration without changing any electronic settings or cables which could effect the detection efficiency. This was made possible by the close proximity of the photodisintegration experiment to the end of the beam line used for the efficiency calibration of the stilbene detector as is schematically indicated in Fig. 3.5.

A ^{6}Li-loaded glass scintillator was the intermediate standard detector against which the stilbene detector was calibrated. The ^{6}Li-loaded glass scintillator is a neutron detector which is simple to use and for which the detection efficiency at energies <0.5 MeV is not sensitive to a bias setting and can therefore be reproduced accurately and easily. The ^{6}Li-loaded glass is increasingly favoured as a standard (Kn83) at low energies.

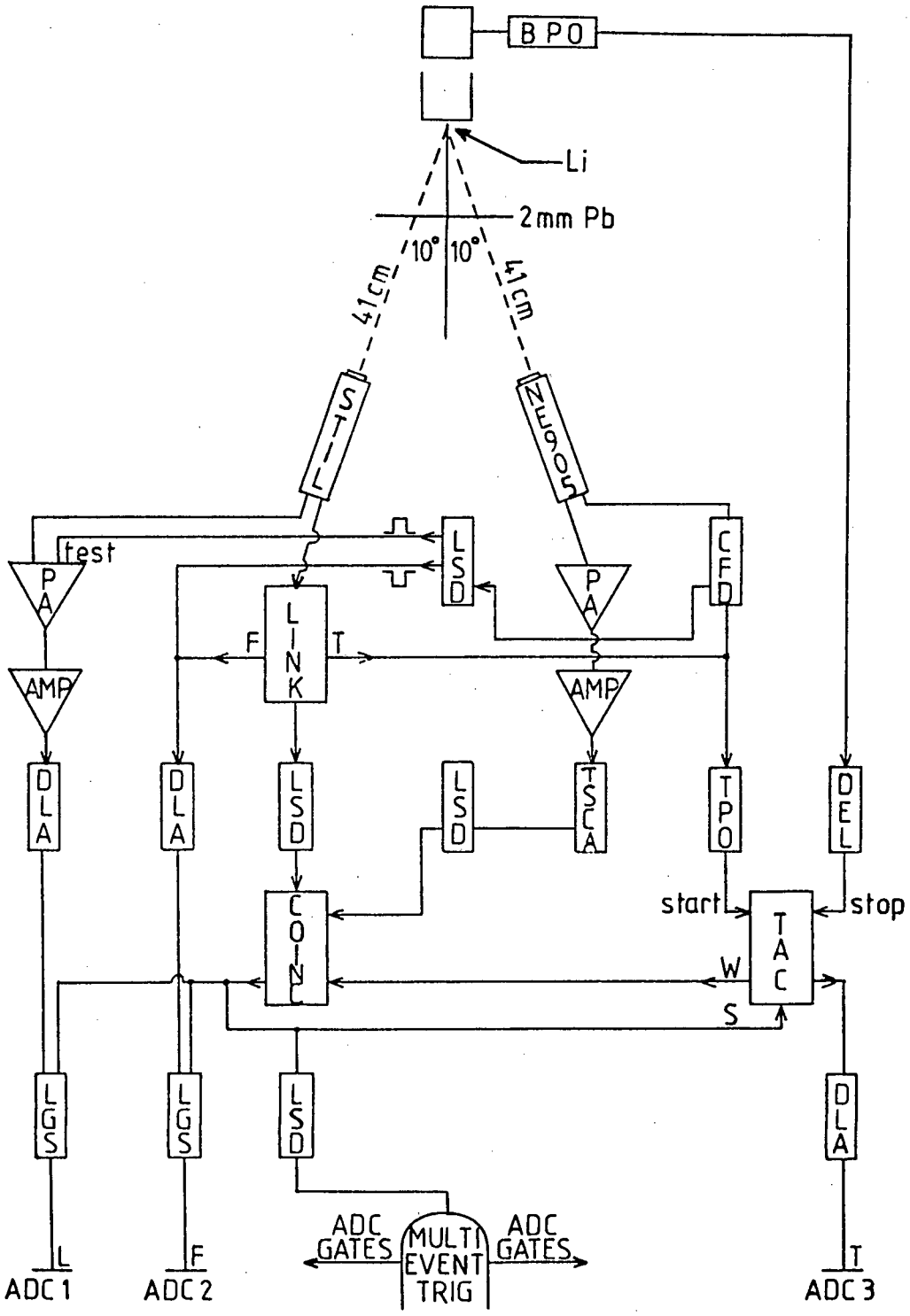

Figure 3.10 A schematic diagram of the geometry and electronic circuit used for the efficiency calibration of the stilbene detector. Key of abbreviations : AMP, amplifier; BPO, beam pick-off; CFD, constant fraction discriminator; COINC, coincidence; DEL, delay; DLA, delay amp; LINK, Link 5010 PSD; LGS, linear gate and stretcher; LSD, logic shaper and delay; PA, preamp; TAC, time to amplitude converter; TPO, time pick-off; TSCA, timing single channel single analyzer.

For detecting neutrons these scintillators make use of the $^{6}Li(n,\alpha)T$ cross section which is well known (La76) (Ga77) (Kn83). Unfortunately there is a broad resonance in the cross section for this reaction centered at 242 keV which is in the energy range of interest (230-270 keV) to this experiment. This was the reason for using the Li glass as an intermediate standard only.

The Li glass was inturn calibrated against a long counter. The long counter has a Hansen and McKibben (Al55) (Al57a) type design. The response of this type of detector over the energy range of interest to the photodisintegration experiments can be considered (to within 2%) as flat (Al57a).

The monoenergetic neutrons needed for the calibration emanated from a thin Li target on a tantalum backing which was bombarded by pulsed (2 nsec rise time) protons from the Van de Graaff. The two detectors were placed (Fig. 3.10) at 10^{o} to the incident beam direction and at an equal distance (both scintillators have the same dimensions) from the target (about 41 cm). The proton energy is known to within 0.1% from monitoring on the beam analyzing magnet with nuclear magnetic resonance and the neutron energies were taken from the Li(p,n) tables in Atomic and Nuclear Data Tables (Li75).

The two main ideas behind the circuit for the stilbene calibration (see Fig. 3.10) were firstly, that the stilbene electronics should be left unaltered from the way it was used in the "normal" mode and secondly, that live time corrections should be eliminated by routing the Li glass into the electronic system of the stilbene detector.

In order to compare the neutron flux detected by these two detectors it is sufficient to have only the time-of-flight spectra for each of the two detectors. The L and F parameters are used to route the Li glass pulses to an unused portion of the F versus L spectra. This makes offline separation of the stilbene and Li glass data easy.

The stop pulses in the time-of-flight parameter came from the beam's stop pulse generator at the Li target. Start signals came from both the stilbene and Li glass detectors. The calibration runs were thus a three parameter experiment namely L, F and T collected event by event on magnetic tape.

3.4.7 Data Acquisition.

The data were acquired via a locally written data acquisition program, SUREAL, running on a PDP-11/34 mini computer. SUREAL can acquire and store multiparameter data event by event in a buffer and write these buffer blocks to tape when full. At the same time single parameter spectra may be accumulated. The multiparameter system can handle a maximum of seven parameters and has four monitors which can display one or two parameter spectra of the data.

The singles spectra are acquired separately and in parallel with the event by event acquisition. Up to seven 4K ADC's or other combinations with the same total memory can be accommodated. Spectra from the monitors and the singles acquisition (save spectra) were written to tape.

Buffer data and save spectra were separately recorded on tapes via the two tape drives available and transferred to the Sperry 1100 mainframe at UCT where further analysis was done.

CHAPTER 4

Data Analysis.

4.1 Introduction.

The data collected for the three series of final runs each consisted of three subsets of data. Two of these subsets, namely the five parameter photodisintegration data collected in "normal" mode and the three parameter neutron efficiency calibration data collected in "calibration" mode were gathered event by event. The separate one parameter gamma spectra from the GeLi detector obtained in the "normal" mode made up the third subset of data.

The three variables evaluated from the analysis of the above mentioned subsets of data were, $N_n(\theta)$, the corrected neutron counts for a particular angle from the photodisintegration data analysis; $\varepsilon_n(E)$, the efficiency of the neutron detector (stilbene) for neutrons of energy E, and N_γ, the corrected gamma counts for a particular angle. These variables together with the factor $\phi_{mc}(\theta)$ from the Monte Carlo calculation of the scattering of neutrons in the deuterated anthracene crystal were used in calculating the differential cross section $\sigma(\theta)$ using the following formula;

$$\sigma(\theta) = [K.\phi_{mc}(\theta).N_n(\theta)]/[k\varepsilon_n(E).N_\gamma] \qquad 4.1$$

where K and k are unknown constants.

The processing of the gamma data is described first (section 4.2). Thereafter the photodisintegration data analysis (section 4.3) is described followed by an account of the analysis of the measurements of the relative detection efficiency of the neutron detector in section 4.4.

The last two mentioned sets of data were measured and analyzed under identical conditions (electronic settings, PSD cuts etc.) to ensure that the detection efficiency measured corresponded to that applying to the photodisintegration experiments. A detailed analysis is shown only for the November series of runs as the same procedure was followed for the September and February series of runs.

4.2 Gamma Analysis.

The 2.75 MeV total energy peak in the gamma spectrum was integrated offline for each run and compared with the peak integral determined at run closure with the use of the SUREAL software. In the latter integration the background under the gamma peaks was determined by calculating the area of the trapezium formed by the counts in the first and the last channels of the integrated peak and the x-axis of the spectra. The background was of the order of 10% of the total peak integral.

The ratio of the offline to online integrals are constant to within 3%. In order to be consistent the online peak areas were used in determining the relative differential cross section as offline integrals were not always available.

There were two corrections applied to the gamma data. A correction for the live time in the GeLi electronics of <5% was applied to the data. The varying of the source angle θ caused a variation in the solid angle of the GeLi detector. In Table 1, the run data for the November data series, the corrected GeLi counts for each run in the November data

Table 4.1 Run Data : November runs

γ-n Angle θ (deg)	Run No.	Time (k sec)	Neutron live time corr. factors	Corr.γ yield (k)
30	5	40.4	1.33	2712
	44	42.1	1.35	3123
	48	36.4	1.40	2926
			Total	8761
45	4	49.3	1.23	1989
	18	40.6	1.32	2966
	35	56.9	1.22	2813
	43	41.0	1.28	2610
			Total	10378
60	3	34.8	1.23	1675
	17	42.8	1.25	2394
	19	55.5	1.24	3186
	41	41.8	1.18	2942
			Total	10197
90	2	45.0	1.18	2165
	16	39.1	1.24	1670
	38	42.5	1.22	2375
	46	41.5	1.28	3470
			Total	9680
120	15	40.0	1.24	2476
	37	42.2	1.35	2629
	42	40.4	1.33	2130
	47	41.4	1.46	3208
			Total	10443
135	14	39.2	1.41	2224
	40	42.0	1.37	1877
	45	42.6	1.52	3052
	49	41.3	1.37	1931
			Total	9084

series can be seen. A small correction (~0.2%) also had to be applied to compensate for this variation.

4.3 The Photodisintegration Analysis.

The processing of the buffer data was done with a programme specially written for the task of scanning data where parameters need to be generated.

The first task was to generate the pulse shape parameter S from the pulse height parameter L and the short pulse integral F for each of the two photoproduct detectors This was done so that optimum PSD cuts could be applied to the data to obtain maximum discrimination against background events. The relationship between the S, L and F parameters used to generate the S parameters is $S = F - KL + C$ where K and C are parameters used to "tune" the PSD.

The value K determines the angles of the γ and n loci in the S vs L distribution. The value of C determines the position of these loci along the S axis. The plot of S vs L shown in Fig. 4.1 for an AmBe source illustrates the quality of separation achieved from this procedure for the stilbene and DA crystals relative to the 60 keV ^{241}Am peak.

For the optimization of the PSD, cuts were made on the S vs L plots of the two detectors as shown in Fig. 4.2. Also shown in Fig. 4.2 are ^{241}Am spectra with the same scale on the L axis as used in the S vs L plots so that one can compare the pulse height of the two detectors. The data were then scanned with these cuts on the S and the L parameters and L_p vs T spectra generated with T the time-of-flight parameter. The deuterated anthracene pulse height parameter L_p was chosen because of its better energy resolution as can

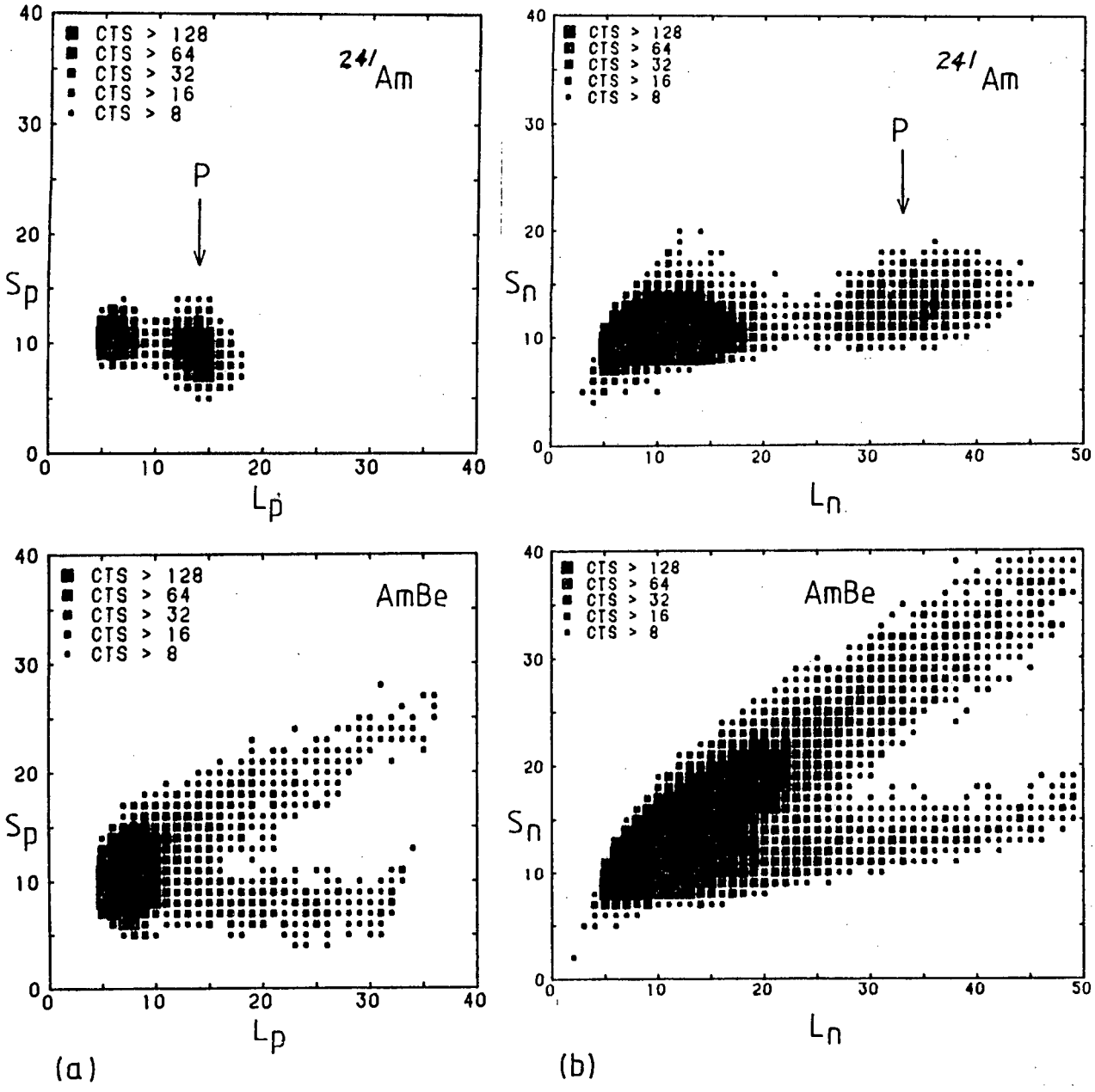

Figure 4.1 Density plots of counts versus pulse height L, and pulse shape S for: a) the deuterated anthracene crystal; b) the stilbene crystal. The upper panels display the 60 keV gamma peak, P, of ^{241}Am. The lower panels show the quality of separation between neutrons and gamma rays with the same scale on the x-axis as the upper panels.

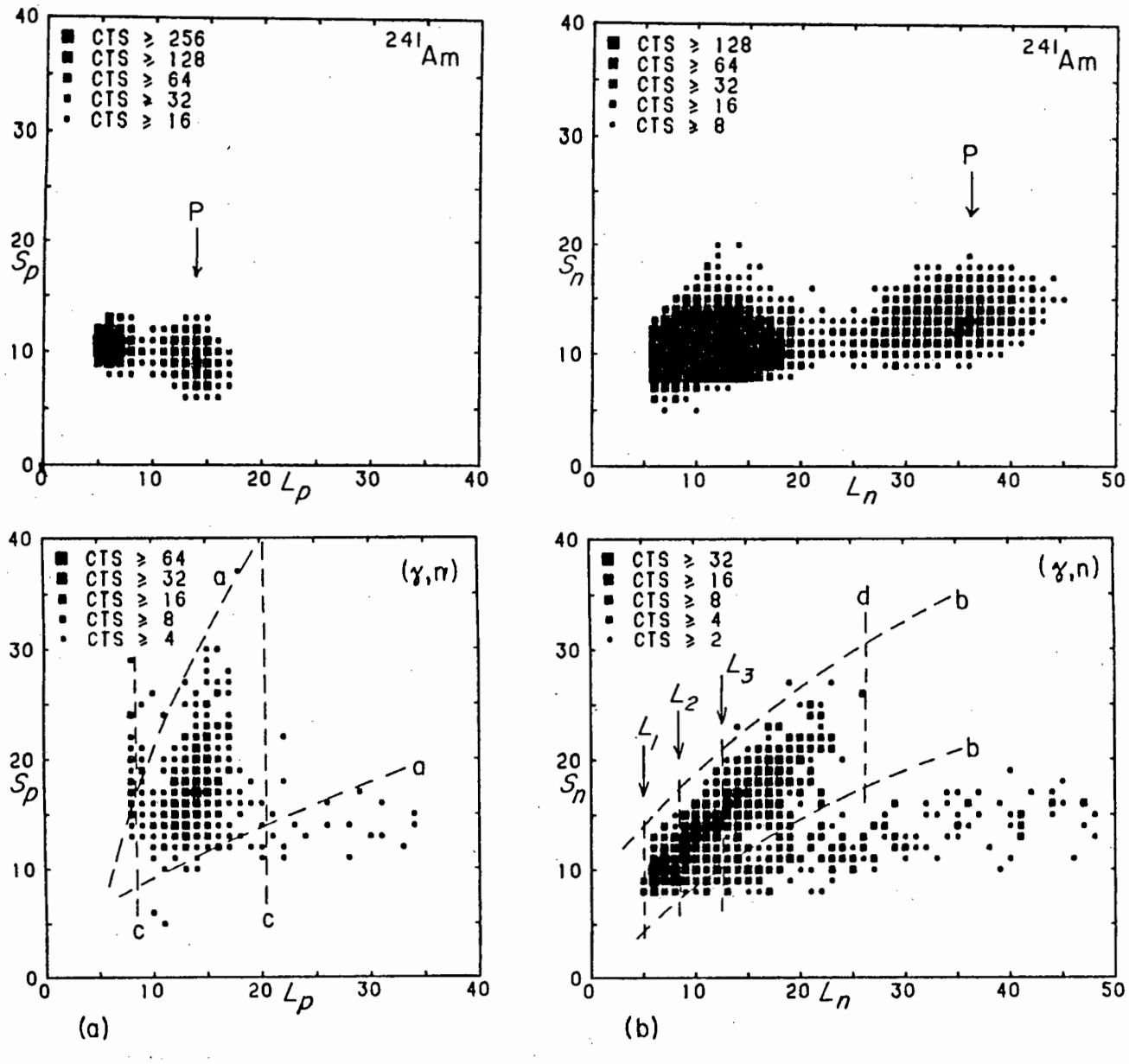

Figure 4.2 Density plots of counts versus pulse height L, and pulse shape S for a) the deuterated anthracene crystal and b) the stilbene crystal. Upper panels display the 60 keV gamma peak of ^{241}Am. The lower panels show the summed 90° data of the Nov. series with cuts a and b, the PSD cuts for photoprotons and photoneutrons respectively; c, the photoproton pulse height cut; and d, together with L_1, L_2 or L_3 the photoneutron pulse height cuts.

be seen from Fig. 4.2. An example of the L_p vs T plots from the November data set for each of the six angles can be seen in Figs. 4.3. to 4.5. The September and February data are similar except for poorer statistics.

There is a clear photoneutron signature well separated from the gamma locus as well as the low pulse height background for every angle θ. This separation along the T axis can be seen to increase with angle as expected. The coincidence requirement incorporated in the experiment was largely responsible for the general background being so low. The background radiation in the room will not be time correlated and so is evenly spread over all times.

Between the lines marked c on the density plots shown in Figs. 4.3 to 4.5 are the sections of the deuterated anthracene pulse height which included the photoneutron peak. These were projected onto the time-of-flight axis. The projected time spectra were used for the calculation of the relative yields of photoneutrons at the measured emission angles.

A composite picture of these projected spectra at each emission angle derived from November series of data can be seen in Fig. 4.6. Two of the three series of time spectra shown in Fig. 4.6 result from different cuts in the stilbene pulse height indicated by L_2 and L_3 in Fig. 4.2. This was done for each set of data, (two cuts in the case of September and February data sets) firstly to check the neutron to gamma ratio which should remain unaffected by such changes and secondly, to determine the best signal to background ratio. Inscattered neutrons (excluding those

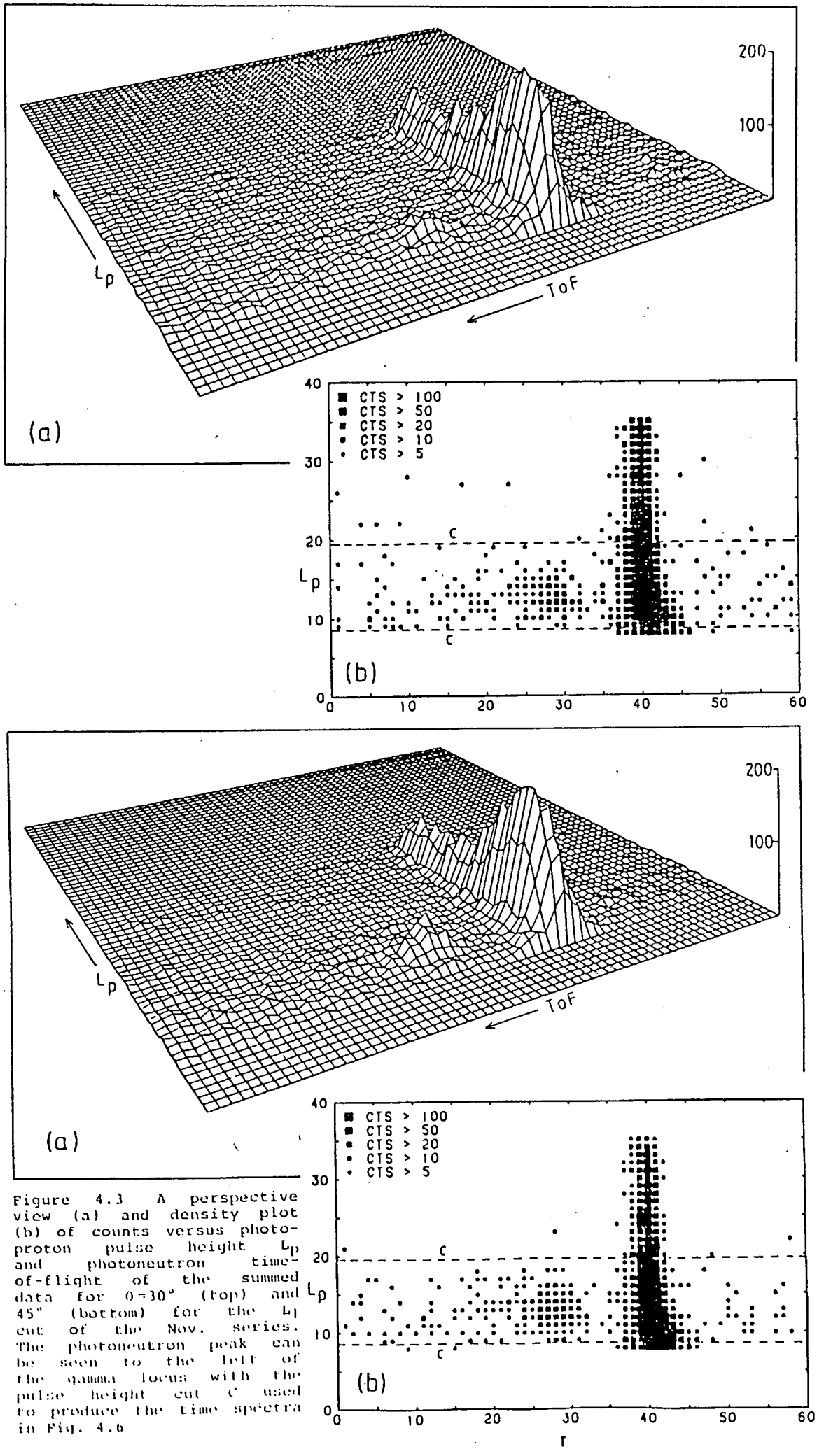

Figure 4.3 A perspective view (a) and density plot (b) of counts versus photoproton pulse height L_p and photoneutron time-of-flight of the summed data for 0-30° (top) and 45° (bottom) for the L_p cut of the Nov. series. The photoneutron peak can be seen to the left of the gamma focus with the pulse height cut C used to produce the time spectra in Fig. 4.6

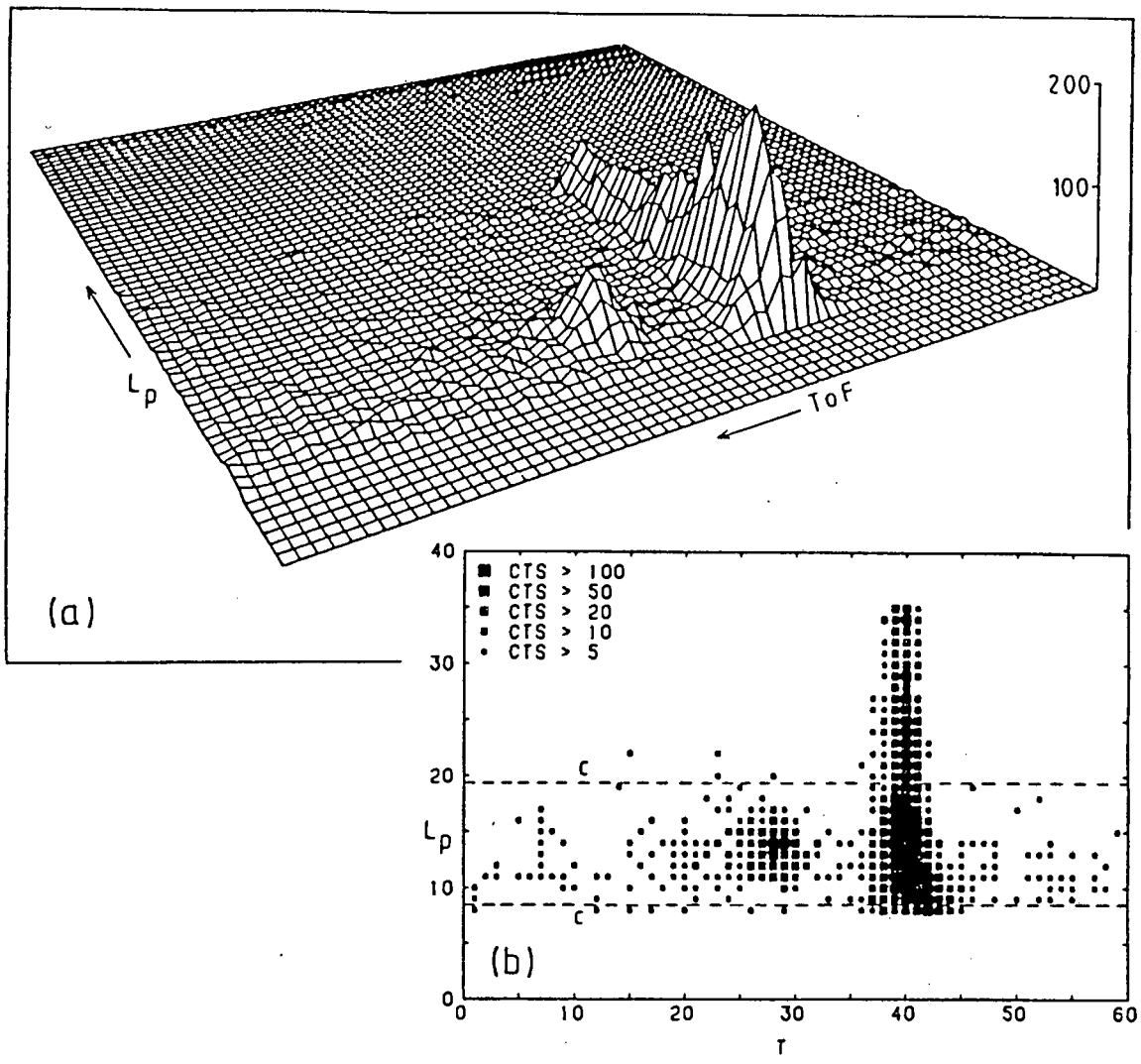

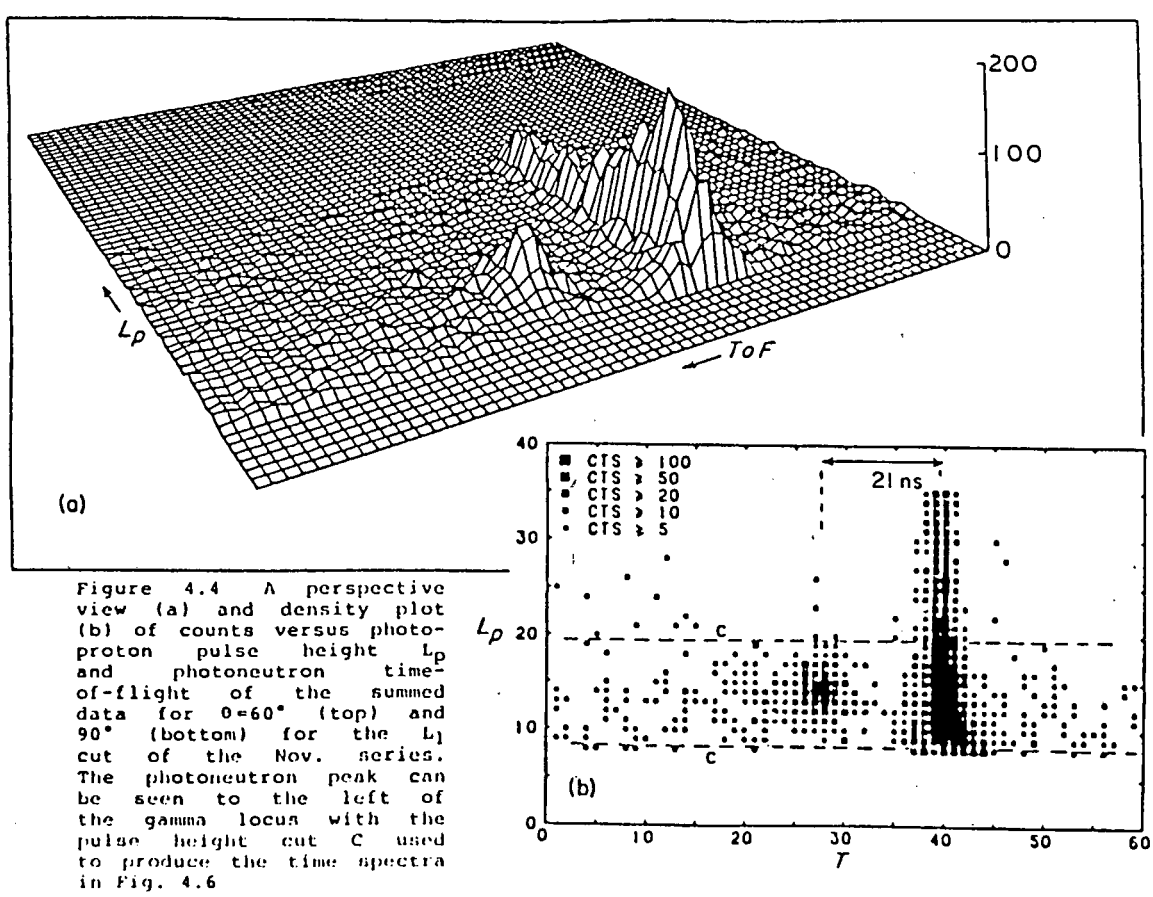

Figure 4.4 A perspective view (a) and density plot (b) of counts versus photoproton pulse height L_p and photoneutron time-of-flight of the summed data for θ=60° (top) and 90° (bottom) for the L_1 cut of the Nov. series. The photoneutron peak can be seen to the left of the gamma locus with the pulse height cut C used to produce the time spectra in Fig. 4.6

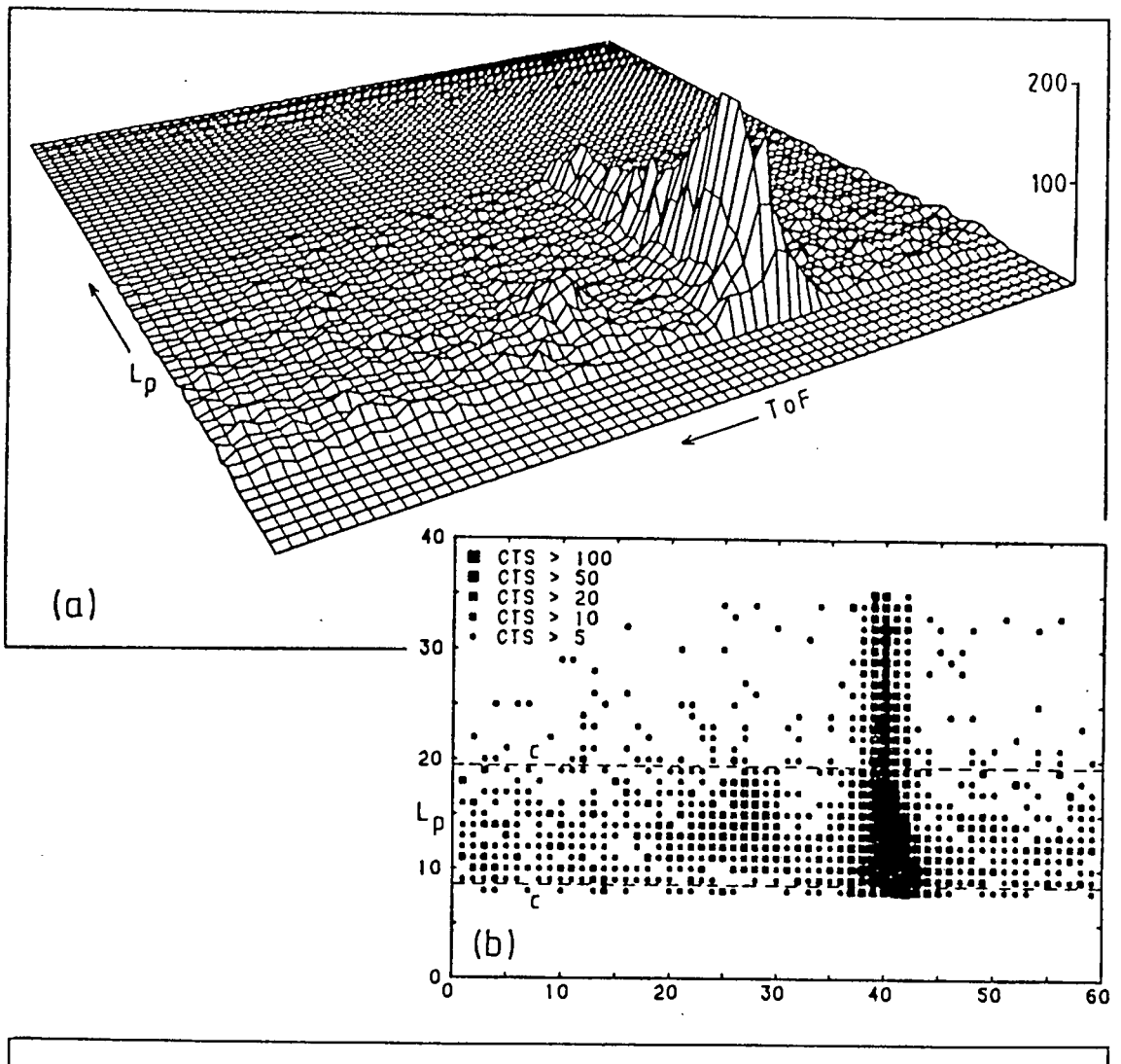

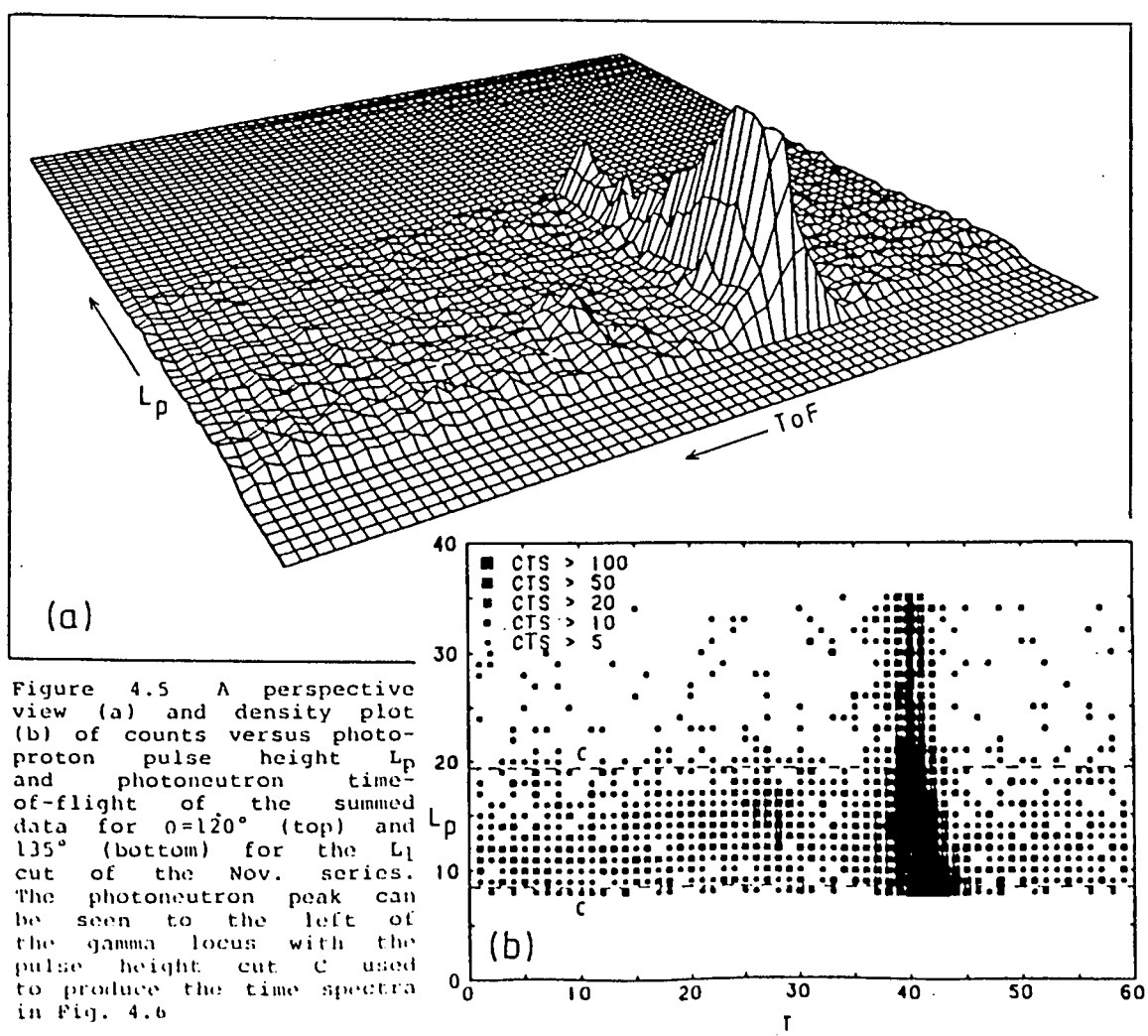

Figure 4.5 A perspective view (a) and density plot (b) of counts versus photoproton pulse height L_p and photoneutron time-of-flight of the summed data for $\theta=120°$ (top) and 135° (bottom) for the L_1 cut of the Nov. series. The photoneutron peak can be seen to the left of the gamma locus with the pulse height cut C used to produce the time spectra in Fig. 4.6

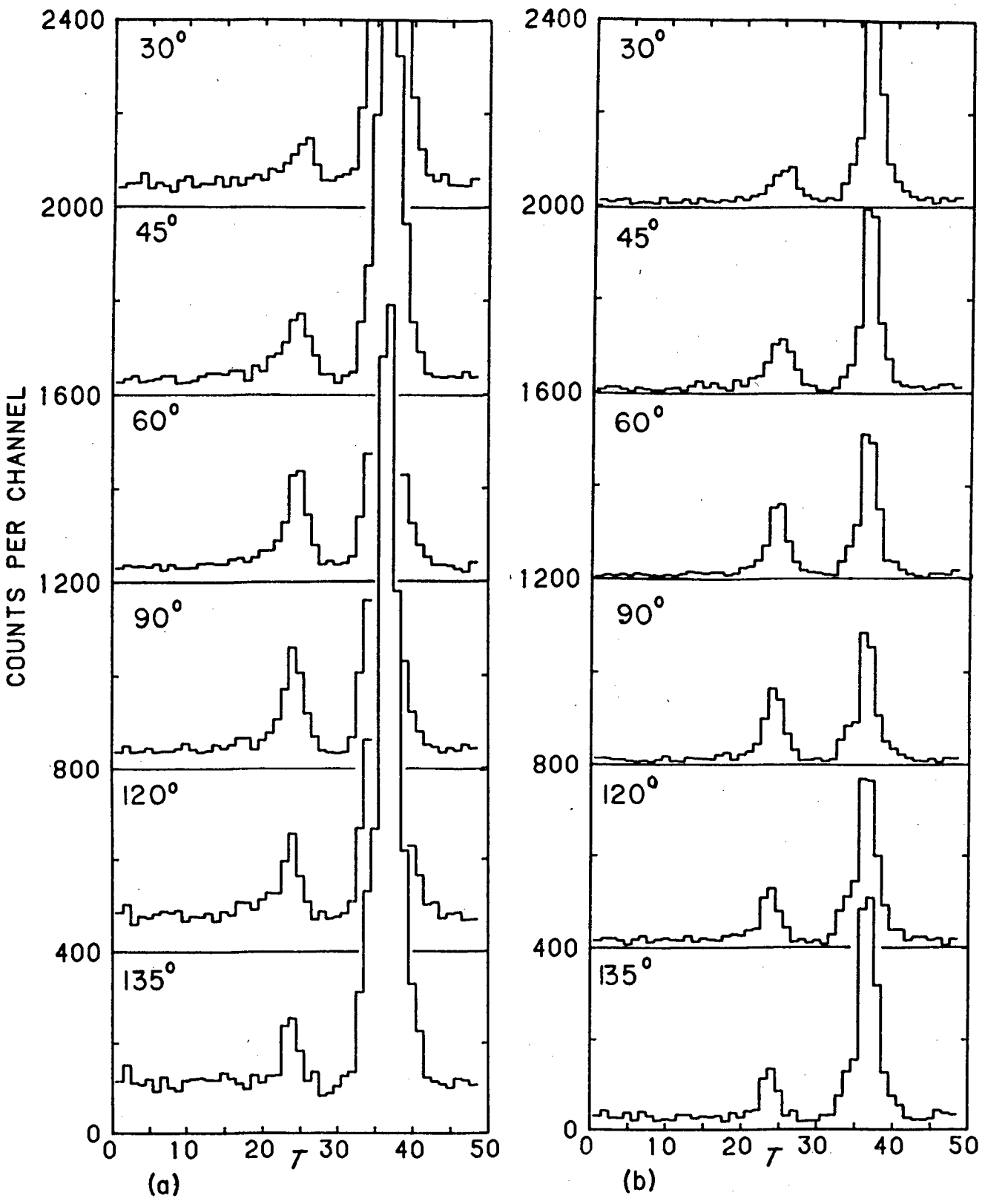

Figure 4.6 A composite plot of time-of-flight spectra at the six angles for cuts L_2 a) and L_3 b) of the November data showing the photoneutron peak, left, and the gamma peak, right. The photoneutron peak has an increased time-of-flight with increase in angle due to the decrease in energy of the emitted photoneutron. Although the background in b) is less than in a) there is also a decrease in the photoneutron counts which is why a) was used for the angular distribution calculation.

scattered in from the deuterated anthracene crystal) will have a longer flight path and would therefore be seen as a tail to the photoneutron peak in the time spectra.

For this reason integrations, N_F, were made in a time-of-flight window over the photoneutron peak. The backgrounds, N_B, for these peaks were determined by the general background levels in these projected time spectra. The difference $N_n = N_F - N_B$ is then the uncorrected neutron count for each run with ΔN_n the uncertainty associated with this count. These values for the summed data at each angle of the November series of data are shown for each of the pulse height cuts (L_1, L_2 and L_3), together with the corresponding efficiency factors ε_n (discussed in the next section), in Tables 4.2, 4.3 and 4.4.

4.4 The Relative Efficiency Determination Of The Stilbene Detector.

The stilbene efficiency calibration (see section 3.3.6) data consisted of three parameter data collected event by event for a series of runs at different neutron energies between 180 and 320 keV. This spanned the range of energies (230 to 270 keV) detected in the photodisintegration experiment (see Fig. 3.9).

In the offline analysis the same cuts which were applied to the photoneutron data, were applied to the calibration data. The analysis generated separated pairs of stilbene and Li glass time-of-flight spectra. An example of this can be seen in Fig. 4.7. The neutron peaks in these spectra were integrated and a ratio of the relative stilbene

Table 4.2 Neutron Yield: November Runs

Cut 1: L_n = 1 - 1600

Θ	N_F	N_B	N_n	ΔN_n	ε_n	N_n/ε_n
30	609	315	294	35	34.2	8.6 ± 1.0
45	912	360	552	41	34.2	16.1 ± 1.2
60	1124	400	724	44	34.2	21.2 ± 1.3
90	1186	330	856	43	33.8	25.3 ± 1.3
120	1380	710	670	53	33.0	20.3 ± 1.6
135	1220	765	455	54	32.7	13.9 ± 1.7

$\Sigma (N_n/\varepsilon_n) = 105.4$

Table 4.3 Neutron Yield: November Runs

Cut 2: L_n = 289 - 1600

Θ	N_F	N_B	N_n	ΔN_n	ε_n	N_n/ε_n
30	416	140	276	28	29.3	9.4 ± 0.9
45	705	145	560	33	29.2	19.2 ± 1.1
60	857	220	637	37	29.0	22.0 ± 1.3
90	898	200	698	37	28.3	24.7 ± 1.3
120	881	375	506	41	27.2	18.6 ± 1.5
135	784	417	367	42	26.7	13.7 ± 1.5

$\Sigma (N_n/\varepsilon_n) = 107.6$

Table 4.4 Neutron Yield: November Runs

Cut 3: L_n = 385 - 1600

Θ	N_F	N_B	N_n	N_n	ε_n	N_n/ε_n
30	313	112	201	24	22.8	8.8 ± 1.1
45	475	80	395	27	22.4	17.6 ± 1.2
60	583	80	503	29	22.0	22.9 ± 1.3
90	596	70	526	29	20.4	25.8 ± 1.4
120	467	105	362	28	18.5	19.7 ± 1.5
135	433	189	244	30	17.7	13.8 ± 1.7

$\Sigma (N_n/\varepsilon_n) = 108.6$

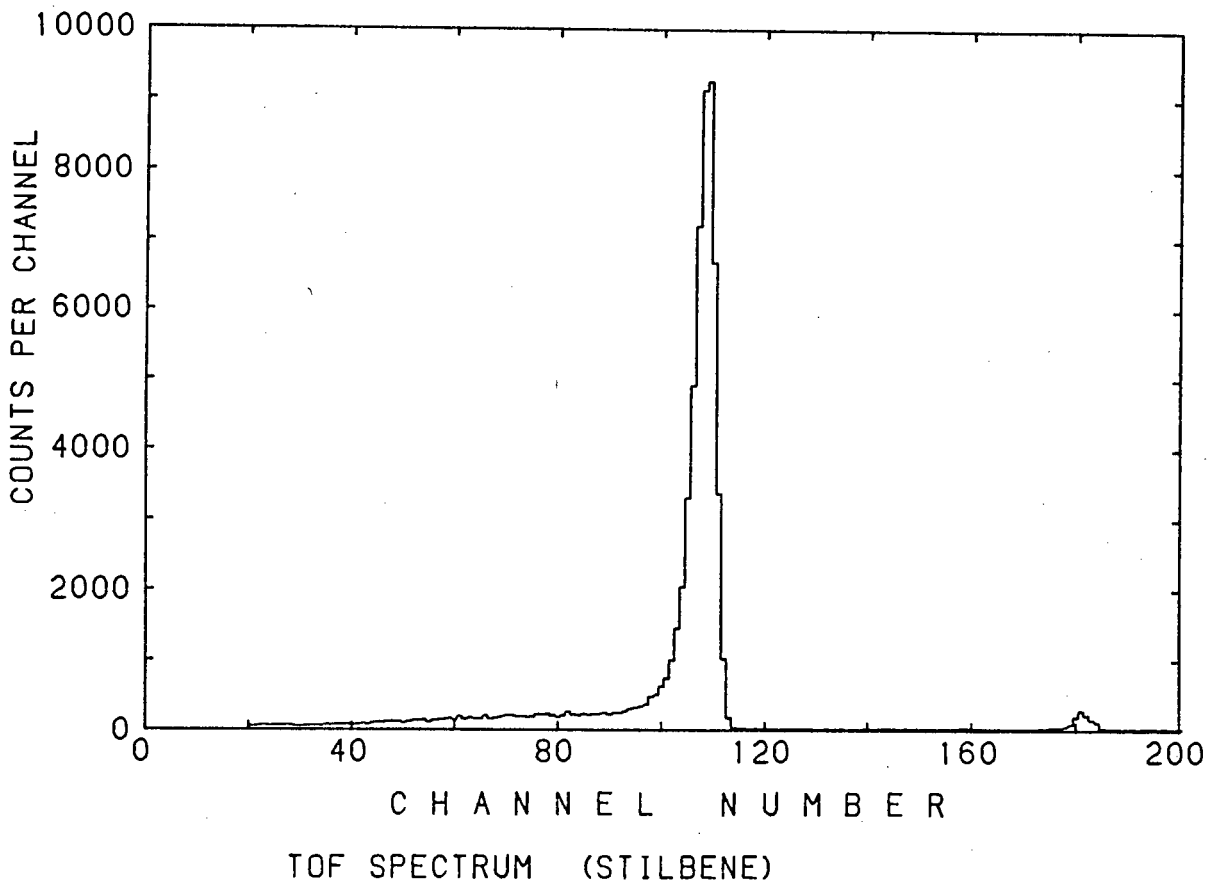

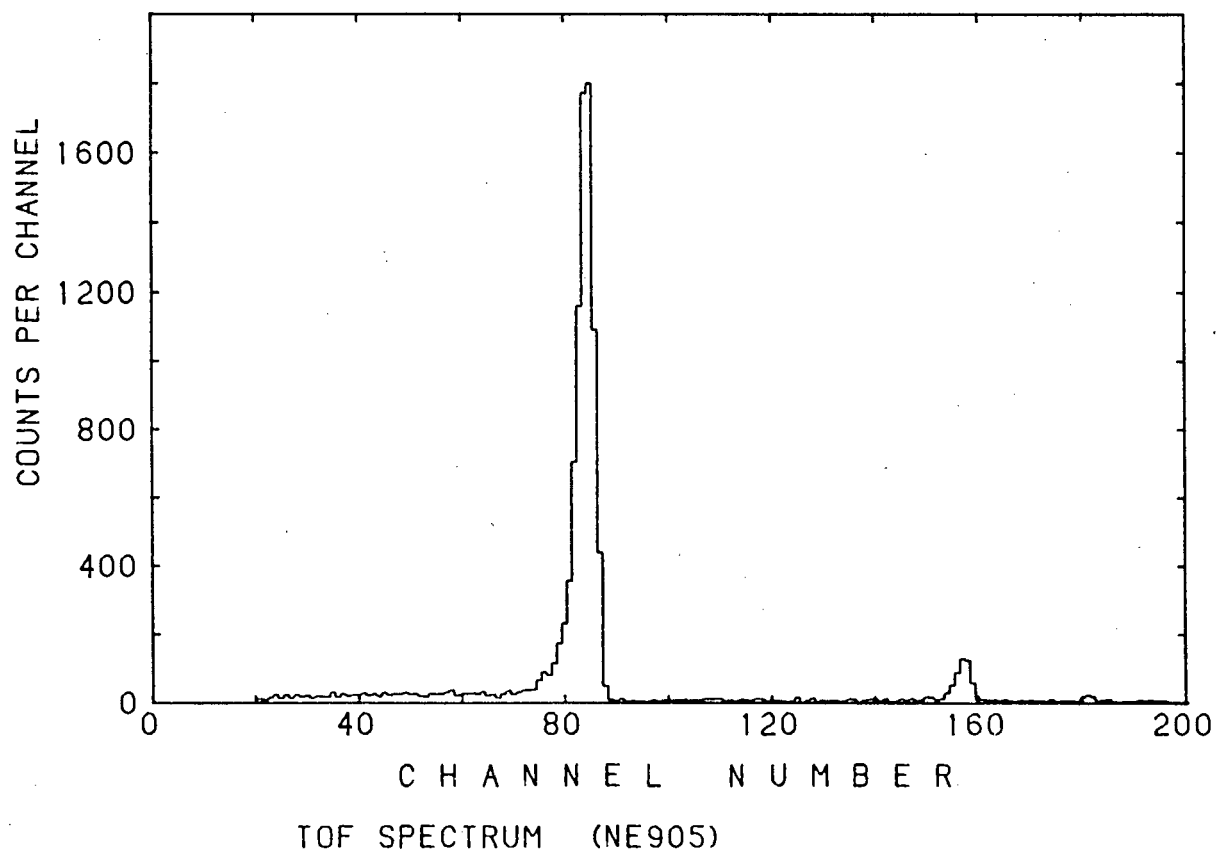

Figure 4.7 Time-of-flight calibration spectra for the stilbene crystal and NE905 Li glass scintillator showing neutrons (left) and gamma rays (right).

to Li glass neutron yield ratio was determined at each energy.

Table 4.5 Neutron Detection Efficiencies

E_n (keV)	Neutron Detection Efficiency ε_n (arbitrary units)							
	NE	Stilbene Detector						
		September		November			February	
	905	cut 1	cut 2	cut 1	cut 2	cut 3	cut 1	cut 2
188	2.25	-	-	27.9	19.8	9.0	-	-
203	3.15	19.3	10.6	30.7	23.0	11.9	17.3	7.54
216	3.84	22.5	14.7	31.4	24.4	14.1	20.0	9.87
229	4.70	24.3	16.0	32.2	26.2	16.9	22.7	12.7
241	5.27	26.6	19.4	32.2	26.0	17.3	25.2	15.1
253	5.67	28.5	21.9	33.0	27.2	19.1	25.7	15.5
266	5.46	31.2	24.4	33.4	27.9	20.5	27.0	18.6
278	5.27	34.9	28.1	34.6	29.0	21.8	29.0	21.0
290	4.58	34.6	28.2	34.7	29.4	22.7	30.9	23.3
301	3.92	33.0	28.1	33.8	29.0	22.9	29.7	22.9
312	3.38	34.3	29.2	-	-	-	-	-
324	2.93	32.8	26.9	33.1	28.7	23.4	30.5	24.8
335	2.56	33.7	29.1	-	-	-	-	-
351	2.18	33.3	28.9	20.6	26.1	21.9	30.0	25.4

The relative efficiency of the stilbene detector ε_n at a particular energy is the product of this ratio and the relative efficiency of the Li glass detector at the energy. Each cut of each series of data was processed in this manner (see Table 4.5) and plotted (see Fig. 4.8). The neutron detection efficiencies of both the stilbene and Li glass scintillators over the energy range of interest can be seen in Table 4.5. The more harsh pulse height cuts are shown, as

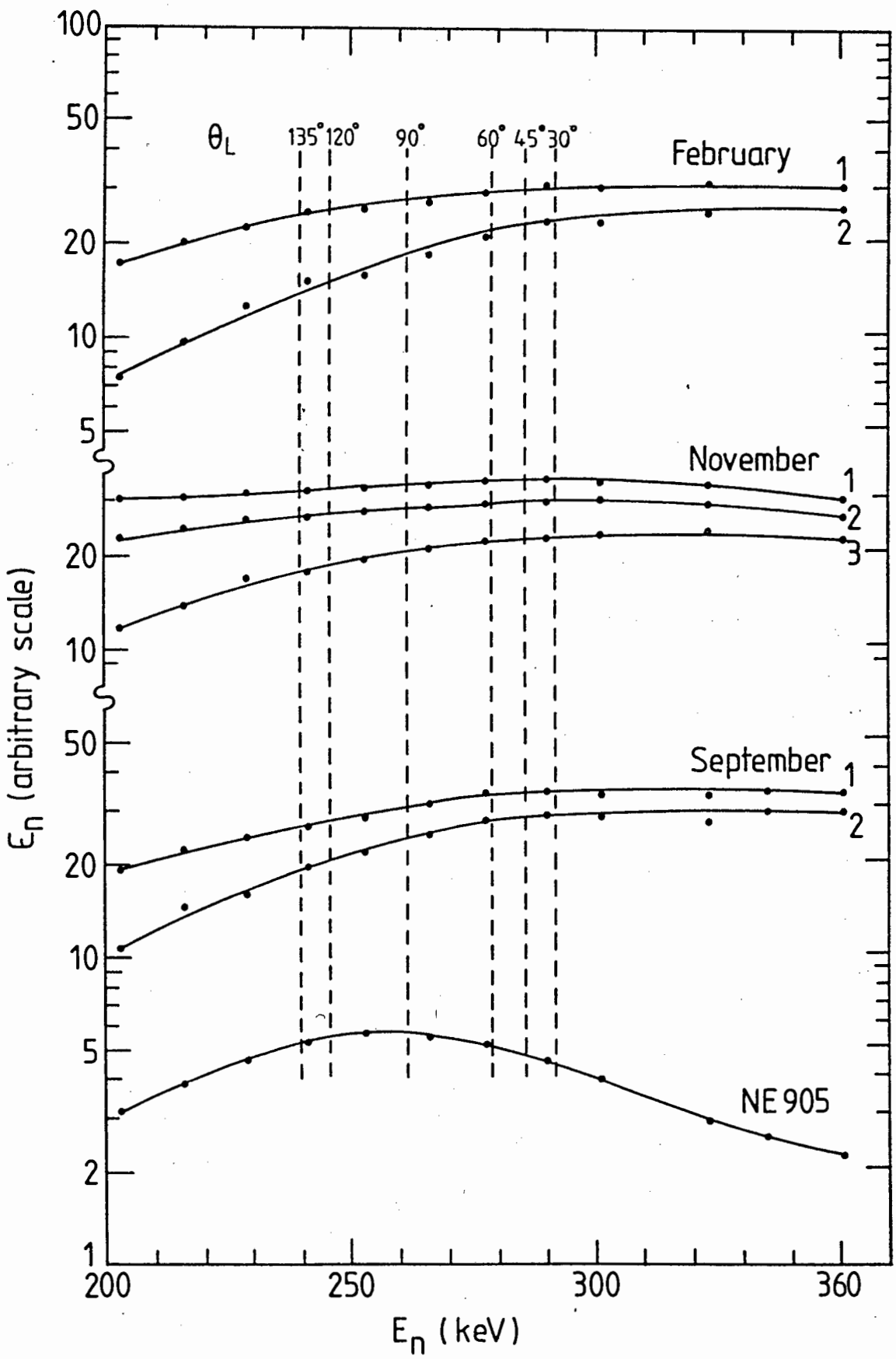

Figure 4.8 Relative stilbene efficiency for the three series of final runs as well as for the NE 905 Li glass scintillator. The statistical errors for the measurements are 4%.

expected, to effect the lower energy neutrons more than those at the top of the energy scale.

From the curves in Fig. 4.8 values for ε_n were read off for the emitted photoneutron energy (see Tables 4.2 to 4.4). These data were used in the calculation of the relative differential cross sections for the three final series of runs which have been tabulated in Tables 4.4 to 4.6).

4.5 Correction factor for multiple neutron scattering in the deuterated anthracene crystal.

Use was made of a Monte Carlo programme$ to simulate the production and scattering of the photoneutrons in the deuterated anthracene crystal. The correction factor, ϕ_{mc}, can take on values both smaller and greater than unity depending on whether a greater number of neutrons were scattered in or out of the angle subtended by the stilbene crystal. The calculated correction factors for the different angles γ-n, θ, are shown in Tables 4.6 - 4.8.

4.6 Summary.

The corrections and adjustments applied in the analysis were: 1. the live time correction and geometrical correction applied to the gamma data. The latter compensates for the gamma source-to-GeLi distances which change with angle θ; 2. the live time correction was introduced as a normalizing factor for each run during the scanning process; 3. an adjustment for the variation in efficiency of the stilbene detector with photoneutron energy (i.e. with photoneutron angle); 4. a correction for multiple neutron scattering within the deuterated anthracene crystal.

$UCT Sperry programme MONTGN (author F. D. Brooks.)

Table 4.6 Angular Distribution: November Data

θ	N_n/ε_n	ϕmc	N_γ	$\sigma(\theta)$
30	8.9 ± 0.9	1.01	8.761	1.03 ± 0.11
45	17.7 ± 1.1	1.05	10.378	1.79 ± 0.11
60	22.0 ± 1.3	1.08	10.197	2.33 ± 0.13
90	25.3 ± 1.3	1.12	9.680	2.92 ± 0.15
120	19.5 ± 1.5	1.12	10.443	2.90 ± 0.16
135	13.8 ± 1.5	1.10	9.084	1.67 ± 0.18
				$\Sigma\ \sigma(\theta) = 11.83$

Table 4.7 Angular Distribution: September Data

θ	N_n/ε_n	ϕmc	N_γ	$\sigma(\theta)$
30	6.46 ± 0.61	1.01	5.061	1.29 ± 0.12
45	11.00 ± 0.76	1.05	5.766	2.00 ± 0.14
60	13.85 ± 0.87	1.08	5.546	2.70 ± 0.17
90	10.91 ± 0.75	1.12	3.480	3.51 ± 0.24
120	7.65 ± 0.76	1.12	3.275	2.62 ± 0.26
135	2.94 ± 0.47	1.10	1.576	2.05 ± 0.32
				$\Sigma\ \sigma(\theta) = 14.17$

Table 4.8 Angular Distribution: February Data

θ	N_n/ε_n	ϕmc	N_γ	$\sigma(\theta)$
30	2.35 ± 0.61	1.01	4.721	0.50 ± 0.13
45	4.06 ± 0.69	1.05	4.582	0.93 ± 0.16
60	6.57 ± 0.79	1.08	6.669	1.06 ± 0.13
90	5.72 ± 0.74	1.12	4.585	1.40 ± 0.18
120	4.22 ± 0.84	1.12	4.601	1.03 ± 0.21
135	2.90 ± 0.75	1.10	4.914	0.65 ± 0.17
				$\Sigma\ \sigma(\theta) = 5.57$

The values for the variables used in equ. 4.1 to calculate the angular distributions for each of the three final series of runs are to be found in Tables 4.6, 4.7 and 4.8.

CHAPTER 5

Results and Conclusions.

5.1 Results

The corrected angular distribution data $\sigma(\theta)$ from the three final series of measurements are summarized in Table 5.1. Columns 2 - 4 of this table shows the final values for each series taken from the right most columns of Tables 4.6, 4.7 and 4.8 respectively and normalized. The coefficient used for each series is the factor required to normalize $\Sigma\sigma(\theta)$ in Tables 4.6 - 4.8 to 12.0. The three series of measurements are therefore presented on the same arbitrary scale in Table 5.1. Column 5 of Table 5.1 shows weighted mean values of the three measurements as a function of angle; weighting being inversely proportional to the square of the estimated uncertainty.

Table 5.1 Normalized Angular Distributions

	$\sigma(\theta)$ (arbitrary units)			
θ	September	November	February	Weighted Average
30	1.09 ± 0.10	1.04 ± 0.11	1.08 ± 0.28	1.07 ± 0.07
45	1.69 ± 0.12	1.82 ± 0.11	1.99 ± 0.34	1.77 ± 0.08
60	2.28 ± 0.14	2.36 ± 0.13	2.28 ± 0.27	2.32 ± 0.09
90	2.96 ± 0.20	2.96 ± 0.15	3.00 ± 0.39	2.96 ± 0.11
120	2.21 ± 0.22	2.12 ± 0.16	2.21 ± 0.45	2.16 ± 0.12
135	1.73 ± 0.27	1.69 ± 0.18	1.39 ± 0.36	1.66 ± 0.14
a/b	0.199 ± 0.024	0.192 ± 0.020	0.184 ± 0.052	0.193 ± 0.015

Figure 5.1a shows the weighted mean values plotted against θ, the angle between the directions of the incident gamma rays and the emitted photoneutrons. The data in this

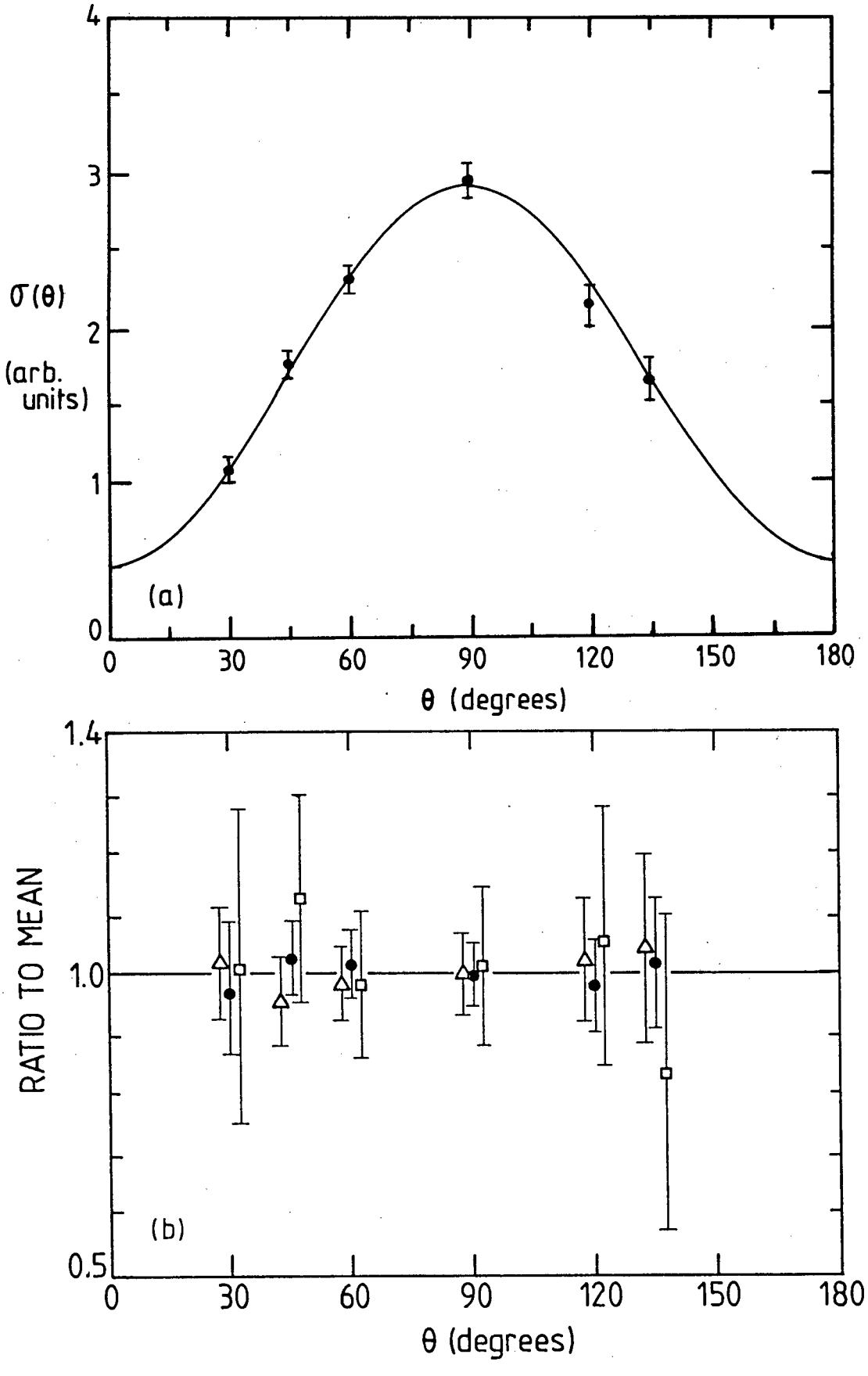

Figure 5.1 Frame a) shows the weighted mean data from column 5 in Table 5.1 plotted against θ, the angle between the directions of incident photons and emitted photoneutrons. Frame b) shows the summed data at each angle for each series of runs (Δ Sept., • Nov. and □ Feb. slightly separated for clarity. In a) the curve represents the best fit using equ. 5.2.

figure show a symmetry about 90^{o} within the statistical uncertainty of the experiment. In Fig. 5.1b the ratio to the mean value of these measurements for each series at each angle, is plotted against θ. The three measurements at each angle can be seen to be consistent (see Fig. 5.1b) within the accuracy of the experiment.

The individual $a/b = 0.199 \pm 0.024$, 0.192 ± 0.020 and 0.184 ± 0.015 for September, November and February respectively. The weighted mean data give $a/b = 0.193 \pm 0.015$ (statistical uncertainty only) and hence $\sigma_m/\sigma_e = 0.290 \pm 0.021$ (calculated using equ. 1.1) namely

$$\sigma_m/\sigma_e = 3a/2b. \qquad 5.1$$

Weighted least square fits (Ly86) of equ. 1.2 namely

$$\sigma(\theta) = a + b\sin^2\theta \qquad 5.2$$

to the angular distribution data were used to obtain these ratios with weighting in inverse proportion to the square of the uncertainty on $\sigma(\theta)$. The fit to the weighted mean $\sigma(\theta)$ data is shown in Fig. 5.1a.

5.2 Discussion

5.2.1 Asymmetry and backward angle measurements.

The abbreviated form (equ. 5.2) of the formula for the angular distribution was used instead of the full form (equ. 2.22) namely

$$\sigma(\theta) = a + b\sin^2\theta + c\cos\theta + d\cos\theta\sin^2\theta + e\sin^2\theta\cos^2\theta \qquad 5.3$$

for the least squares fit to the present data. The reason for this is that the c and d terms of equ. 5.3 describe an asymmetry of the data about 90^{o} and the data are symmetrical about 90^{o} to within the limits of accuracy of the measurement. The e term is expected to be negligibly small (Ru84).

weighted mean data shown in Fig. 5.1a. There is little or no asymmetry to be seen at this level of accuracy.

Forward angle data only were used by Rustgi et al. (Ru83) because no published data at this energy with backward angle measurements were available and, to the best of our knowledge, are still not. Some of the old experiments could not discriminate between forward and backward angles and in the Bishop measurement the angle was inferred from the energy, but this distribution was not shown.

5.2.2 A comparison to published data.

The calculated σ_m/σ_e ratios have for comparison been plotted in Fig. 5.3 together with previous measurements at this energy on an arbitrary x-axis to separate them. The present new σ_m/σ_e ratio is in good agreement with most of the old values which includes the measurements of Meiners (Me49) and Genevese (Ge49). Those being the exception are the measurements of Woodward et al. (Wo49) and Bishop et al. (Bi51a) which are respectively the highest and lowest values.

Woodward and Halpern's measurement was done with a bremsstrahlung end point method which, because of the continuous gamma spectrum used, makes, as has been pointed out in chapter 1, background calculations difficult.

Bishop's measurement (the publication can seen in Appendix A) has the lowest σ_m/σ_e ratio and thus lowest isotropic component. This low isotropic component is common to the set of three values reported in Bishop's paper (See Table 1.1).

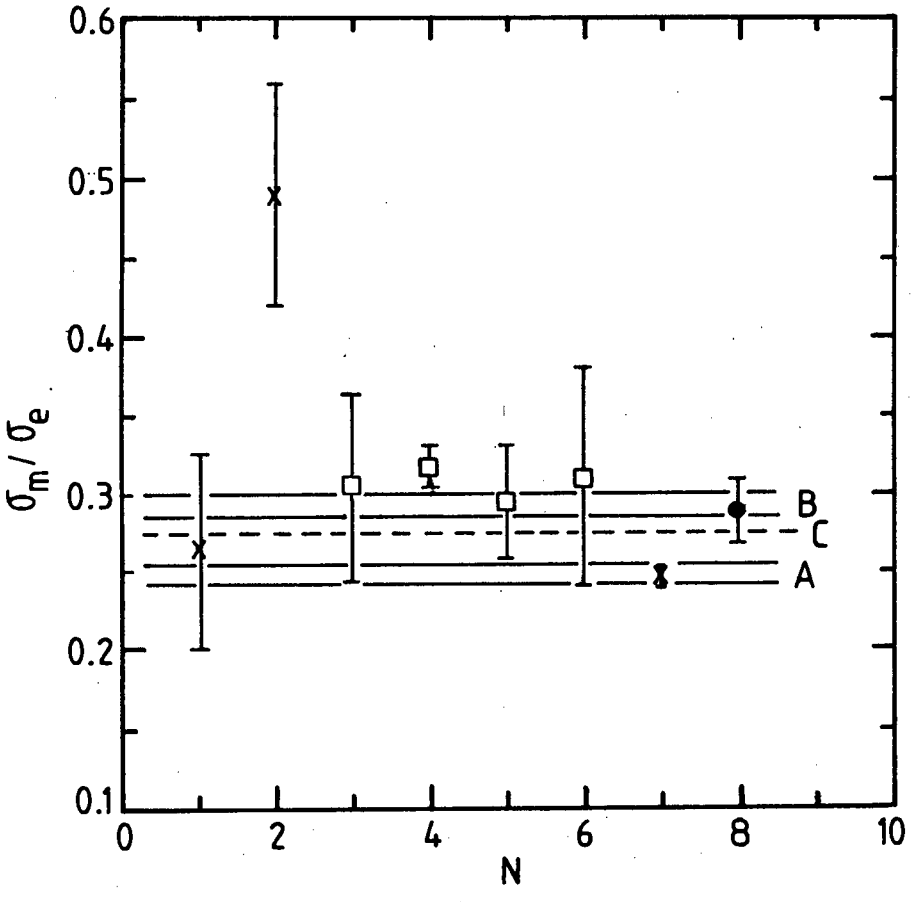

Figure 5.3 A display of the data and calculations of the dipole cross section σ_m/σ_e at E_q = 2.75 MeV. The character used denotes the particle detected namely crosses for protons squares for neutrons and the circle is the present n-p coincidence measurement. The data are identified by the arbitrary ordinate N with; 1 (La49), 2 (Wo49), 3 (Me49), 4 (Me49), 5 (Ge49), 6 (Ha49), 7 (Bi51a) and 8 the present measurement. The lines represent calculations with (B Hamada-Johnston potential, (Ar74) and C Paris potential, (Mi86))and without (A (Be50)) MEC and IC contributions.

The Bishop measurements agreed with the non meson exchange current theory (see Fig 5.3) and had the smallest error bars as well as also being the last measurement made at this energy. The lack of interest in the threshold energy region has possibly been partly due to these measurements being considered as definitive and in good agreement with theory of the day.

5.2.3 MEC and IC contributions.

Including explicit meson exchange current contributions in calculations for the total cross section calculations for radiative capture of neutrons by protons at thermal energies, the inverse photodisintegration reaction at lower energies, has proven successful (Ri72) in explaining the long standing 10% discrepancy between theory and experiment. MEC effects should therefore be evident in the threshold region for deuteron photodisintegration.

Lines B and A in Fig. 5.3 are theoretically predicted values for σ_m/σ_e with (Ar73) and without (Be50) meson exchange currents respectively. Line C in this figure is from privately communicated calculations with meson exchange currents and isobar configurations (MEC and IC) by Miller and Arenhövel (Mi86). The calculations for line C were made using the more modern Paris potential as apposed to the Hamada-Johnston potential used in the calculations on which line B is based.

There have been no published calculations of σ_m/σ_e with meson exchange currents explicitly included at these energies. Arenhövel et al. (Ar73) however, did calculations for the $D(\gamma,n)$ reaction with and without MEC and IC effects at these energies using the Hamada-Johnston potential and presented σ_T, $\sigma(\theta)$ and $P(\theta)$ resulting from their calculations. A plot taken from their paper showing this can be seen in Fig. 5.4.

It can be seen from this plot that the contribution from isobar configurations to the total cross section at E_γ =

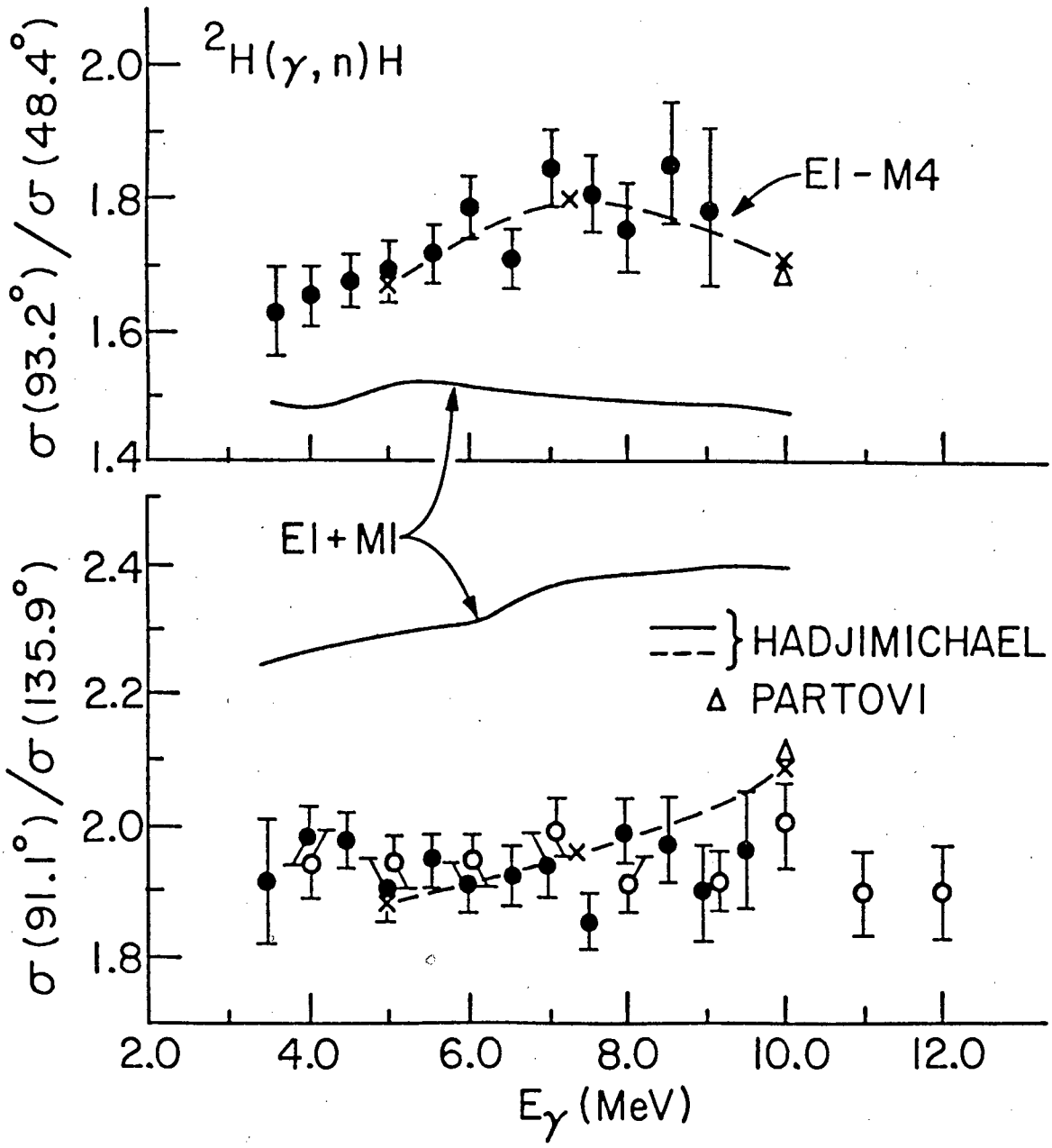

Figure 5.5 The solid and open circles represent data taken at 10- and 19 MeV by Holt (Ho81). The dashed curves representing calculations which included multipoles up to L=4, is shown to be a better fit to the data than curves representing calculations with E1 and M1 multipoles only.

5.2.5 Polarization.

Jewell et al. (Je65) have measured the angular distribution of the polarization of neutrons from the D(γ,n) reaction at E_γ = 2.75 MeV from 30° to 150°. They discuss their data with reference to the theoretical approximation of Kawaguchi (Ka58). Assuming no contributions from either D state photodisintegration or MEC and IC effects, Kawaguchi shows that the nucleon polarization P(θ) is given by

$$P(\theta) = \frac{(\frac{2}{3})^{\frac{1}{2}}(a/b)^{\frac{1}{2}}\sin[\delta(^1S) - \delta(^3P)]\sin\theta}{(a/b) + \sin^2\theta} \qquad 5.4$$

where a and b are the same coefficients as used in the angular distribution equations and $\delta(^1S)$ and $\delta(^3P)$ are the phase shifts for the ^1S_o and ^3P states for n-p scattering. It is through the S and P states that photodisintegration predominantly proceeds for magnetic and electric dipole transitions respectively. Since $\delta(^1S)$ and $\delta(^3P)$ are well determined the polarization measurements may be used in conjunction with equ. 5.4 to determine a value of a/b and hence σ_m/σ_e. A value of σ_m/σ_e much lower than any of the dipole cross section ratios determined from angular distribution measurements (see Table 1.2) is required. The experimentally measured P(θ) data (Je65) are therefore in disagreement with values calculated from equ. 5.4 using any value of a/b within the range of experimentally measured values of this quantity.

Recent and more accurate calculations of P(θ) by Rustgi et al. (Ru83a) (see Fig. 5.6) which include D-state and two-

body charge- and current-density effects are in disagreement by 18% with the data of Jewell et al.. This disagreement still exists.

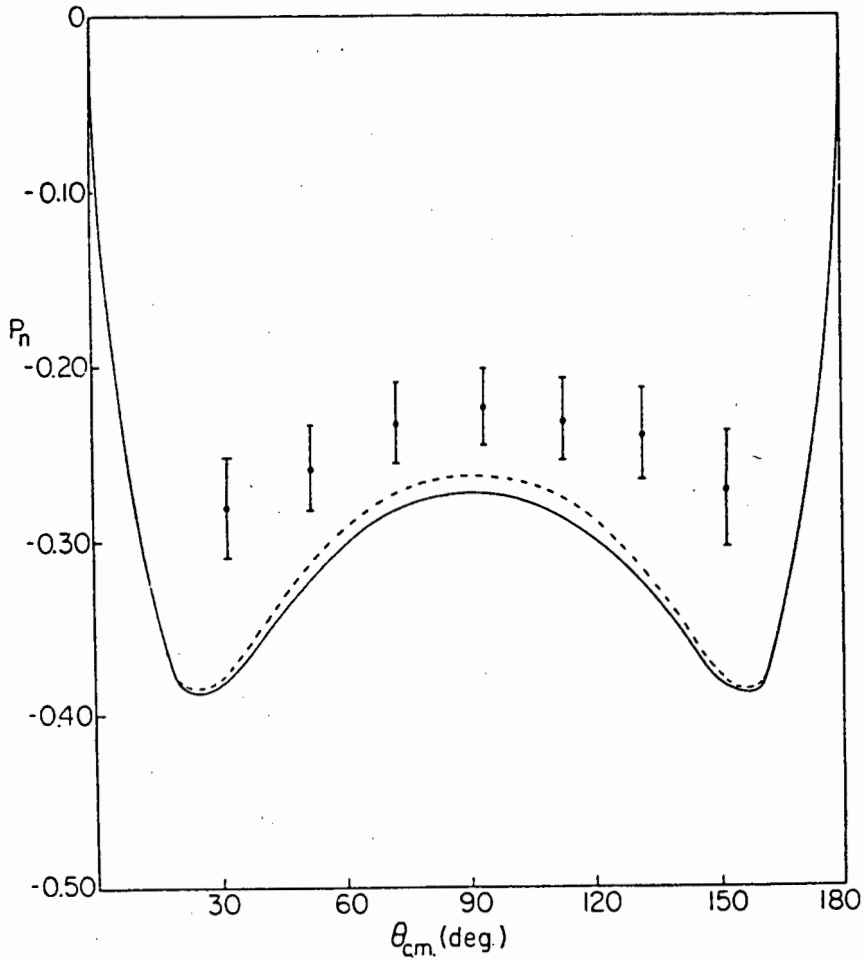

Figure 5.6 The polarization data of Jewell et al. (Je65) compared to calculations by (Ru84) for a SSC-B potential with (solid curve) and without (dashed curve) two-body charge and current effects.(Figure from (Ru83a))(refer to Fig. 2.5)

5.3 Conclusion.

The angular distributions measured in this work give a σ_m/σ_e value of 0.290 ± 0.021 (statistical uncertainty) at E_γ = 2.75 MeV. It is expected that the systematic errors have been kept down to the per cent level. This value agrees with some of the older measurements which support the enhancement in the calculated total cross section due to MEC and IC effects and disagrees with the measurement of Bishop.

At the Workshop on Radiative Processes TRIUMF in Canada (Di84), the need for accurate photodisintegration measurements in the low energy region was recognized by several different speakers (Ca84)(Hw84)(Ru84). This measurement may therefore be seen as a step towards meeting this need. This method can also be used at other energies in the region of this measurement.

Accurate measurements made over an even wider range of angles than the present measurement at this energy are needed. Through the E1 component being suppressed at 0^{o}, a lot can be learned from studying this reaction at 0^{o}. Such an experiment is feasible and can be made using the present setup with a weak source and a long running period.

Absolute angular distribution measurements at these energies are also needed. The absolute calibration of neutron detectors are however difficult. By doing an absolute efficiency calibration of a Li glass detector via an associated particle experiment and then using it as in the present experiment, absolute measurements at these energies could possibly be made.

It can be expected that the exact description of the NN force, even at these low energies, will not be exactly known until the deeper lying structure of the nucleons and there interaction with the structures of other nucleons is understood. Given the present discrepancies between data and theory, there is a clear need for more precise total cross section, polarization and angular distribution measurements for the $D(\gamma,n)$ reaction in the threshold energy range. The combined information from these observables for the $D(\gamma,n)$

reaction in this energy range has not yet realized its full potential as a probe for the long range interaction of the NN force.

REFERENCES

(Ad78)J M Adams and G White, Nucl. Instr. and Meth., 121 (1978) 459.

(Al57)Iu A Aleksandrov, N B DeLone, L I Slovokhotov, G A Sokol and L N Shtarkov, Zh. Eksperim. i Teor. Fiz. 33 (1957) 614 (Translation in Sov. Phys. -JRPT 6 (1958) 472).

(Al57a)W D Allen and A T G Ferguson, Proc. Phys. Soc. A70 (1957) 6359.

(Al55)W D Allen, A.E.R. Report NP/R (1955) 1667.

(Ar74)H Arenhövel, W Fabian and H G Miller, Phys. Lett. No. 3 52B (1974) 303.

(Ar81)H Arenhövel, Phys. Rev. Lett. No.10 47 (1981) 749.

(Ba71)J E E Baglin, E J Bentz and R W Carr, Bull. Amer. Phys. Soc. 16 (1971) 649.

(Be35)H A Bethe and R E Peierls, Proc. Roy. Soc. A148 (1935) 146.

(Be50)H A Bethe and C Longmire, Phys. Rev. No. 5 77 (1950) 647.

(Be56)H A Bethe and P Morrison, Elementary nuclear theory 2nd Ed. (J Wiley and sons New York, 1956) p. 75.

(Bl63)J M Blatt and V F Weisskopf, Theoretical nuclear physics, (J Wiley and sons New York, 1963) p. 601.

(Bi51a)G R Bishop, L E Beghian and H Halban, Phys Rev. 83 (1951) 1052.

(Bi51)G R Bishop, H Halban, P F D Shaw and R Wilson, Phys. Rev. No. 2 81 (1951) 219.

(Bi57)G R Bishop and R Wilson, in Handbuch der Physik, ed. S Flugge, vol. 42 (Springer-Verlag Berlin, 1957) p. 309.

(Bo63)R Bösch, J Lang, R Muller and W Wolfli, Helv. Phys. Acta 36 (1963) 657.

(Br36)G Breit and E U Condon, Phys. Rev. 49 (1936) 904.

(Br57)F D Brooks, Nucl. Instr. and Meth. 4 (1959) 904.

(Br74a)F D Brooks and D T L Jones, Nucl. Instr. and Meth. 121 (1974) 69.

(Br74)G E Brown and A D Jackson, The nucleon nucleon interaction, (Nordita Denmark, 1973) p. 1.

(Ca82)A Cambi, B Mosconi and P Ricci, Phys. Rev. Let. No. 7 48 (1982) 462.

(Ca84)J M Cameron, Can. Jour. Phys. 62 (1984) 1019.

(Ca85)J M Cameron, still to be published S. A. Jour. Phys.

(Ch34)J Chadwick and M Goldhaber, Nature 134 (1934) 237.

(Ch37)J Chadwick, Feather and Bretcher, Proc. Roy. Soc. A163 (1937) 366.

(Ch71)M Chemtob and M Rho, Nucl. Phys. A163 (1971) 1.

(Ci84)CINDA 84, CINDA-B and CINDA-A vol. 1 (IAEA Press Vienna)

(Ci59)M Cini, S Fubini and A Stanghellini, Phys. Rev. 114 (1959) 1633.

(Cl84)F Close, The cosmic onion; Quarks and the nature of the universe, (Heinemann educational books London, 1984) p. 46.

(De59)J J de Swart, Physica 25 (1959) 233.

(De84)J J de Swart, Nuc. Phys. A416 (1984) 299c.

(Di84)Final discussion, Can. Jour. Phys. 62 (1984) 1122.

(Er84)T E O Ericson, Nuc. Phys. A416 (1984) 281c.

(Fe51)H Feshbach and J Schwinger, Phys. Rev. No. 2 84 (1951) 194.

(Fr84a)J L Frair, B F Gibson and G L Payne,Phys. Rev. C No. 2 30 (1984) 441.

(Fr84)J L Frair and S Fallieros, Phys. Rev. C 29 (1984) 1645.

(Ga77)D B Gayther, Ann. Nucl. Energy 4 (1977) 515.

(Ge49)F Genevese, Phys. Rev. No. 9 76 (1949) 1288.

(Gr45)G A R Graham and H Halban, Rev. of Mod. Phys. No. 2 & 3 17 (1945) 297.

(Ha49)B Hamermesh and A Wattenberg, Phys. Rev. 76 (1949) 1408.

(Ha62)T Hamada and I D Johnstone, Nuc. Phys. 34 (1962) 382.

(Ha73)E Hadjimichael, Phys. Let. No. 2 46B (1973) 147.

(Ha80)E Hadjimicheal and D P Saylor, Phys. Rev. Lett. 45 (1980) 1776.

(Ho80)K Holinde, Phys. Rep. No. 3 68 (1980) 121.

(Ho81)R J Holt, I E E E Trans. on Nuc. Sci. No. 2 NS-28 (1981) 1279.

(Ho83)R J Holt, K Stephenson and J R Specht, Phys. Rev. Lett. No. 8 50 (1983) 577.

(Hu53)L Hulthen and B C H Nagel, Phys. Rev. No. 1 90 (1953) 62.

(Hu57)L Hulthen and M Sugawara, Handbuch der Physik ed. S Flugge, vol. 39 (Springer-Verlag, Berlin, 1957) p. 1.

(Hu76)R J Hughes, A Zieger, H W Caffler and B Ziegler, Nuc. Phys. A 267 (1976) 329.

(Hw84)W Y P Hwang, Can. Jour. Phys. 62 (1984) 1019.

(Ja75)H E Jackson, R J Holt and W M Wilson, Ann. Rep. A.N.L. 75-75.

(Ja76)H E Jackson, R J Holt, R M Lazewski and W M Wilson, Ann. Rep. A.N.L. 76-96.

(Ja79)H E Jackson, R J Holt, G Mavrogenes and J R Specht, Ann. Rep. A.N.L. 79-40.

(Je65)R W Jewell, W John, J E Sherwood and D H White, Phys. Rev B139 (1965) 71.

(Ka58)M Kawaguchi, Phys. Rev. 111 (1958) 1314.

(Kn83)H -H Knitter and Budtz-Jørgenson, Nucl. data for Science and Tech., ed. K. H. Bockhoff, (D Reidel Publ. Comp. Holland 1983) p. 451.

(La48)N O Lassen, Phys. Rev. 74 (1948) 1533.

(La49)N O Lassen, Phys. Rev. 75 (1949) 1099.

(La76)G P Lamaze, O A Wasson, R A Schrack and A D Carlson, Proc. of the Intern. Conf. on the Interaction of Neutrons with Nuclei, 2 (1976) 1341.

(La77)G P Lamaze, Symp. on Neutron Standards and Applications NBS-SP 493 (1977) 37.

(La80)M Lacombe, B Loiseau, J M Richerd, R Vinh Mau, J Cote, P Pires and R de Tourriel, Phys. Rev. C, No. 3 21 (1980) 861.

(Li75)H Liskien and A Paulsen, Atomic and Nucl. Data Tables 15 (1975) 57.

(Ly86)L Lyons, Statistics for nuclear and particle physicists, (Cambridge Univ. Press, 1986).

(Mc56)W R McMurray, Ph.D. Thesis (Oxford Univ. 1956).

(Me49)E P Meiners, Phys. Rev. No. 2 76 (1949) 259.

(Mi86)H G Miller and H Arenhövel, Private communication.

(My42)F E Myers and L C van Atta, Phys. Rev. 61 (1942) 19.

(Na72)R Nath, F W K Firk, and H L Schultz, Nucl. Phys. A 194 (1972) 49.

(No72)H P Noyes, Ann. Rev. Nucl. Sci. 22 (1972) 465.

(Pa64)F Partovi, Ann. Phys. 27 (1964) 79.

(Ra41)W Rarita and J Schwinger, Phys. Rev. 59 (1941) 436.

(Re83)U Reus and W Westmeier, Atomic and Nucl. Data Tables 29 (1983) 13.

(Ri72)D O Riska and G E Brown, Phys. Lett. No. 4 38B (1972) 193.

(Ro67)R R Roy and B P Nigam, Nuclear physics Theory and experiment (J Wiley and sons New York, 1967)

(Ru60)ML Rustgi, W Zernik, G Breit and D J Andrews, Phys. Rev. No. 5 120 (1960) 1881.

(Ru83)M L Rustgi, R D Nunemaker and R D Sharma, I L Nuovo Cimento No. 3 77 (1983) 317.

(Ru83a)M L Rustgi, R Vyas and M Chapra, Phys. Rev. Lett. No. 4 50 (1983) 236.

(Ru84)M L Rustgi, R Vyas and O P Rustgi, Phys. Rev. C. No. 3 29 (1984) 785.

(Sa51)E E Salpeter, Phys. Rev. No. 1 82 (1951) 60.

(Sc47)J S Schwinger, Phys. Rev. 72 (1947) 724.

(Sh70)Y M Shin, J A Rawlins, W Buss and A O Evwaraye, Nuc. Phys. A154 (1970) 482.

(Si35)A J F Siegert, Phys. Rev. 52 (1937) 787.

(Sq52)G L Squires, Prog. in Nuc. Phys. 2 (1952) 89.

(Ur32)H C Urey, F G Brickweddle and G M Murphy, Phys. Rev. 40 (1932) 1.

(Vi47)F Villars, Helv. Phys. Acta 20 (1947) 476.

(We71)B Weissman and H L Schultz, Nuc. Phys. A174 (1971) 129.

(Wh58)A L Whetstone and J Halpern, Phys. Rev. 109 (1958) 2072.

(Wo49)W M Woodward and I Halpern, Phys. Rev. No. 1 76 (1949) 107.

10 MAR 1987